TECHNISCHE UNIVERSITÄT WIEN

DIPLOMARBEIT

Reactive Sputtering of Dense Yttria-stabilized Zirconia

zur Erlangung des akademischen Grades

Diplom-Ingenieur

im Rahmen des Studiums

Masterstudium Physikalische Energie- und Messtechnik

eingereicht von

Florian Dolezal, BSc
Matrikelnummer 11802536

ausgeführt am Institut für Chemische Technologien und Analytik
der Fakultät für Technische Chemie der Technischen Universität Wien

Betreuer:
Univ.Prof. Dipl.-Phys. Dr.rer.nat. Jürgen Fleig
Senior Scientist Dr.techn. DI Tobias Huber
Projektass. Dipl.-Ing. Dr.techn. Alexander Schmid

Wien, 23.02.2024

(Unterschrift Verfasser) (Unterschrift Betreuer)

Abstract

Yttria-stabilized zirconia (YSZ) is an O^{2-} ion conducting material via vacancy hopping. This property enables the use of YSZ as a typical electrolyte in solid oxide fuel cells. However, this ability is also interesting for the use in thin film oxygen ion batteries. In both applications, YSZ thin films are attractive in order to achieve low cell resistance. In this work, two methods to deposit YSZ thin films were tested. One method was reactive radio frequency magnetron sputtering and the other was reactive direct current magnetron sputtering. The produced thin films were analyzed by electrochemical impedance spectroscopy, scanning electron microscopy, X-ray fluorescence spectroscopy, grazing incidence X-ray diffraction and laser induced breakdown spectroscopy. Furthermore, profilometer measurements were conducted to evaluate the thin film thickness.

In the course of the sputter depositions, a process to reproducibly generate electronically insulating YSZ thin films over the whole sputtered area was developed. The crucial aspect of the preparation procedure involves conducting two distinct sputter depositions with a cleaning step in between. This process resulted in approximately 800 nm thin films with a yttria content of about 9.3 mol%.

The developed procedure was used to successfully produce a thin film oxygen ion battery. The battery was repeatedly charged and discharged with currents between 10 to 1000 µA at a temperature of 350 °C. The contribution of the electrolyte to the overpotential of the battery was estimated to be less than 20 %.

Kurzfassung

Yttrium-stabilisiertes Zirkoniumdioxid (YSZ) ist ein O^{2-} Ionen leitendes Material, ermöglicht durch Sprünge in Sauerstoff Leerstellen. Diese Eigenschaft ermöglicht die Verwendung von YSZ als typischen Elektrolyten in Festoxid-Brennstoffzellen. Diese Fähigkeit ist aber auch für den Einsatz in Dünnschicht-Sauerstoffionenbatterien interessant. In beiden Fällen sind YSZ Dünnschichten attraktiv, um einen geringen Zellwiderstand zu erreichen. In dieser Arbeit wurden zwei Methoden zur Abscheidung von YSZ-Dünnschichten getestet. Eine Methode war das reaktive Hochfrequenz-Magnetron-Sputtern, die andere Möglichkeit das reaktive Gleichstrom-Magnetron-Sputtern. Die hergestellten Dünnschichten wurden mittels elektrochemischer Impedanzspektroskopie, Rasterelektronenmikroskopie, Röntgenfluoreszenzspektroskopie, Diffraktometrie unter streifendem Einfall und laserinduzierter Plasmaspektroskopie analysiert. Weiters wurden Profilometermessungen zur Ermittlung der Schichtdicken durchgeführt.

Im Zuge der Sputterabscheidungen wurde ein Verfahren zur reproduzierbaren Erzeugung elektronisch isolierender YSZ-Dünnschichten über den gesamten gesputterten Bereich entwickelt. Der entscheidende Aspekt des Herstellungsverfahren ist die Durchführung von zwei getrennten Sputterabscheidungen mit einem dazwischen liegenden Reinigungsschritt. Dieser Prozess führte zu etwa 800 nm dicken Dünnschichten mit einem Yttriumoxidgehalt von etwa 9.3 mol%.

Das entwickelte Verfahren wurde zur erfolgreichen Herstellung einer Dünnschicht-Sauerstoffionenbatterie genutzt. Die Batterie wurde mehrfach mit Strömen zwischen 10 und 1000 µA geladen und entladen bei einer Temperatur von 350 °C. Der Beitrag des Elektrolyten zum Innenwiderstand der Batterie wurde auf weniger als 20 % geschätzt.

Contents

1 Introduction

The rise in population and growing household incomes are driving an increase in the energy demand. However, the energy sector still heavily relies on fossil fuels. This dependency leads to the emission of greenhouse gases and in consequence to global warming [1]–[3]. Continuous utilization of fossil fuels will lead to erratic weather patterns, an elevation in sea levels, significant health impacts, loss of biodiversity, etc. [4], [5]. In order to stop climate change, renewable energies which emit almost no greenhouse gasses such as solar energy, wind energy, biomass, biofuels, etc are of major importance for the future of the energy sector [6]. Many of the renewable energy sources depend on irregular natural conditions. Therefore, it is necessary to store the produced energy to meet the demand and stabilize the grid. One way to achieve this is through methods such as electrochemical energy storage (like batteries) or by generating clean hydrogen [7]–[9].

Solid oxide fuel cells (SOFCs) hold significant promise in facilitating the transition from fossil fuels to renewable energies. Especially the possibility of using various fuels and a fuel-to-power conversion efficiency that can exceed the efficiency of the Carnot cycle are advantages of SOFCs [1], [10]. The fuel flexibility enables the use of different biogases stemming from biomass, a vital renewable resource [11]–[13]. Another promising technology are reversible SOFCs with two operation modes. One mode is the SOFC mode, where hydrogen is transformed into water while producing heat and power. The other mode is the solid electrolyzer mode. In this mode, water is split into hydrogen and oxygen through the input of heat and electricity ideally stemming from renewable energy for example solar energy [7], [14].

1.1 Fundamentals of SOFCs

Essentially a SOFC consists of two porous electrodes that are separated by an electrolyte. Figure 1 shows an illustration of a SOFC and the occurring reaction. Air or oxygen is supplied as an oxidant to the cathode where the oxygen is reduced

$$O_2 + 4e^- \rightarrow 2\,O^{2-}. \tag{1}$$

The anode is supplied with fuel, for example hydrogen, that gets oxidized

$$2\,H_2 + 2\,O^{2-} \rightarrow 2\,H_2O + 4e^- \tag{2}$$

resulting in two electrons and water as a byproduct. The electrolyte is an oxygen ion conductor, typically yttria-stabilized zirconia (YSZ), that prevents the gases from mixing and enables the transport of the oxygen ions to the anode. On the other hand, it is a bad electron conductor which results in the flow of electrons through an external circuit. Using hydrocarbons as fuel is also an option. However, in these cases, only hydrogen undergoes electrooxidation, facilitated by the chemical reformation of the hydrocarbons. One major disadvantage is the high operating temperature between 800-1000 °C to electrically and ionically activate the materials. This leads to a high degradation of the cells and high system costs [15]–[18].

To reduce the cost and increase the stability, the operating temperature can be decreased to 600-800 °C. However, this reduces the ionic conductivity of the electrolyte. One

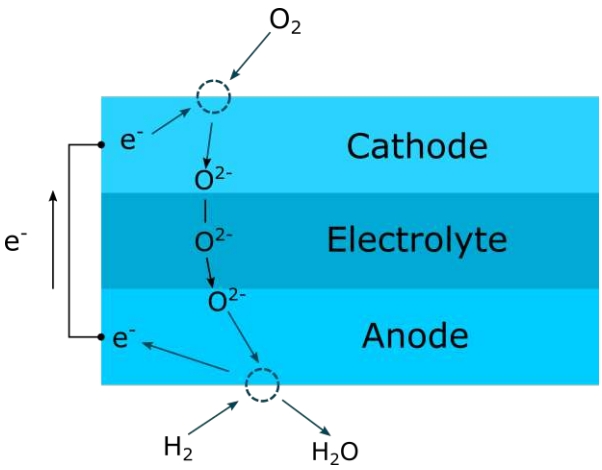

Figure 1: Working principle of a SOFC [19].

common way to reduce the resistance of the cell is a reduction of the thickness of the electrolyte through physical vapor deposition techniques [20]–[22].

1.2 Oxygen Ion Battery

A new technology for stationary energy storage to stabilize the grid or for the use in high-temperature environments are oxygen ion batteries with a working temperature between 350-500 °C. They consist of two mixed ionic and electronic conducting (MIEC) perovskite-type oxides as electrodes and an oxygen ion conducting electrolyte, for example YSZ. The MIEC electrodes can change the oxygen (non)stoichiometry by applying a voltage. This ability is described by the chemical capacitance. It is possible to store electric energy by altering the oxygen levels within a MIEC electrode through the flow of a current and the prevention of oxygen exchange with the atmosphere. By combining two electrodes with different reducibility, it is possible to form a battery. Oxygen can be transported from one electrode to the other through the transport of oxygen ions across the electrolyte. However, the electrolyte blocks this path for the electrons due to a high electronic resistance. The battery can be discharged by enabling a flow of electrons through an external circuit or charged by applying a voltage. The benefits of this technology compared to other batteries are the use of non-inflammable and mostly abundant materials for the battery.

One possibility to increase the performance of oxygen ion batteries is the reduction of the internal electric resistance. The usage of a YSZ thin film instead of a single crystal as an electrolyte can cut down the ionic resistance by orders of magnitude by reducing the distance traveled by the ions [19].

1.3 Aim of the Thesis

Physical vapor deposition methods are often used to prepare thin films due to the high reliability and repeatability. One common way to deposit YSZ thin films is magnetron sputtering [20]. In the field of SOFCs, several studies already showed the possibility of

preparing YSZ electrolytes by sputter-deposition. Here, the substrate is usually a porous electrode and operation temperatures $\geq 700\,^{\circ}\mathrm{C}$ [21], [23]–[25].

The aim of the thesis, on the other hand, is the development of a procedure for the reproducible preparation of dense YSZ thin films via reactive radio frequency or reactive direct current magnetron sputtering as an electrolyte for oxygen ion batteries. Here, an operation temperature of about $350\,^{\circ}\mathrm{C}$ is aimed at. Therefore, it is necessary to prevent pinholes over the whole sputtered area to prevent an electronic short circuit between the electrodes.

2 Theory

2.1 Sputtering

Sputtering is a physical vapor deposition (PVD) process. By bombarding a solid surface, called the target, with energetic ions atoms can be ejected. This is called sputtering. The sputtered atoms can deposit onto the substrate to produce a thin film [26].

Many different effects occur on the surface due to the bombardment of the ions. The bomarding particles can for example eject secondary electrons, get reflected as high energy neutrals, or be implanted into the surface. They also lead to a collision cascade, where a transfer of parts of the momentum to the surface can occur and possibly eject a surface atom. However, over 95% of the energy transferred generates heat.

Typically the target is cooled to reduce the radiant heat and restrain diffusion, which is especially important when using an alloy target. The flux of sputtered atoms only has the same composition as the target when the target is sputtered layer by layer. In this case, the more volatile atoms are sputtered more which leads to an enrichment of the sputter target surface by the material with lower sputtering yield and therefore to a flux of the same composition as the bulk of the target.

One typical way to generate high-energy particles for the bombardment is the generation of plasma and the acceleration of the positive ions to the target through a negative potential of the target with respect to the plasma. A common gas for sputtering is argon because it is rather inexpensive and inert [27]. In Figure 2 an example of a sputtering configuration is shown.

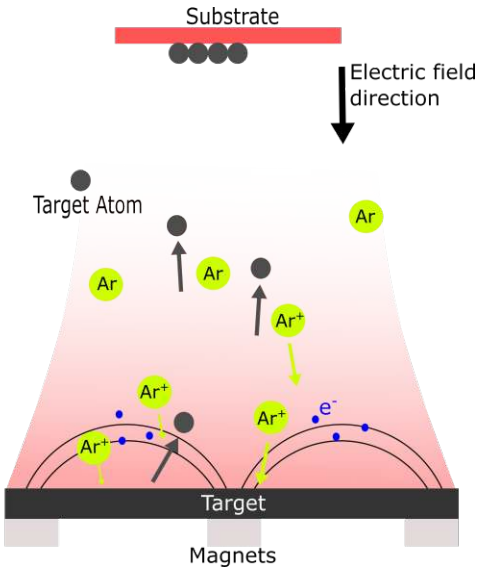

Figure 2: Schematic of a sputtering configuration.

To increase the sputtering yield magnetron sources are frequently used. Permanent magnets create field lines parallel to the target, thus confining secondary electrons through the Lorentz-Force close to the target. This results in a higher gas ionization, augmented flux of bombarding particles and therefore to a higher deposition rate. In this study,

a balanced magnetron configuration is used. This setup uses a ring of magnets at the edge of the target and a magnet in the center [28]. However, this setup also leads to the formation of a racetrack, an area exhibiting a higher sputtering yield compared to other areas of the target. Figure 3 shows an example of a racetrack on the target [27].

Figure 3: Metallic YSZ target with circular racetrack.

2.1.1 Radio Frequency (RF) Sputtering

The common frequency for RF sputtering is 13.56 MHz. At this frequency, the electrons gain enough energy to ionize the atoms and generate a plasma. During one half wave, the surface potential is negative and the ions accelerate toward the target. During the other half wave, the surface potential is positive and the electrons bombard the target surface. This process also occurs at the substrate surface. Due to the higher electron velocity of the electrons target and substrate accumulate a negative charge, which leads to a negative potential with respect to the plasma. This results in a sputtering process on both surfaces. In order to achieve a film growth on the substrate, the target potential has to be larger than the substrate potential. This can be achieved through the grounding of the substrate.

One advantage is the possibility of sputtering insulating materials due to the capacitive coupling of the target to the plasma. However, there are also drawbacks to RF Sputtering. One major drawback is a low sputtering rate and interferences due to the radio frequency. Furthermore, during the use of insulating targets large thermal gradients can lead to cracking of the target due to low thermal conductivity [27], [29].

2.1.2 Direct Current (DC) Magnetron Sputtering

The cathode, also known as the target, is at a negative potential whereas the substrate resides on the anode and is at ground potential. This generates a DC diode discharge.

The secondary electrons ejected from the cathode are captured by the magnetrons to build up a high-density plasma, serving as a source for the ion bombardment. For DC sputtering a conductive target is necessary, because otherwise the target will accumulate a surface charge, which prevents sputtering.

2.1.3 Reactive Sputter Deposition

It is also possible to deposit insulating thin films by sputtering a metallic target. For this purpose, it is necessary to introduce a second gas besides Ar. This second reactive gas, for example, O_2 or N_2, reacts with the sputtered atoms at the film surface to form the desired compound. However, the reactive gas can also form a compound on the surface of the target and "poison" the target. This should be prevented by adapting the amount of reactive gas because it reduces the deposition rate [27].

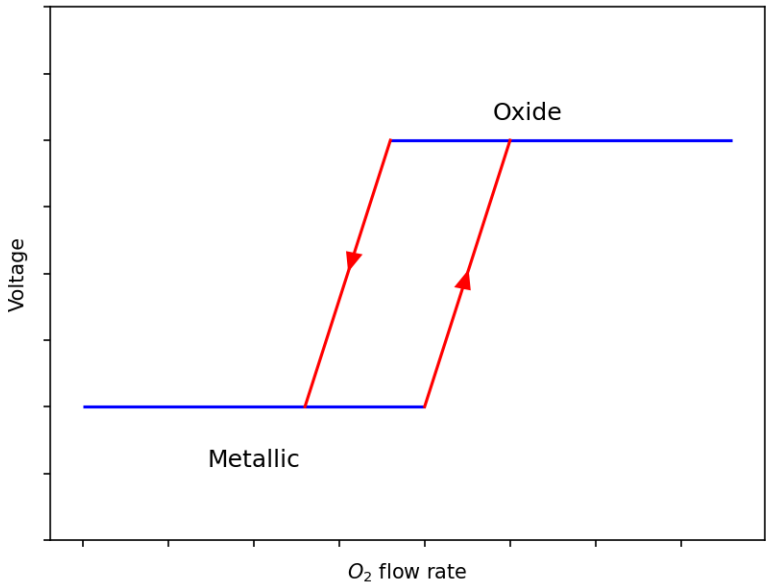

Figure 4: Schematic of the target voltage vs the oxygen flow rate.

Figure 4 illustrates the behavior of the voltage when the current is constant and the reactive gas flow is modified. The introduced oxygen can be adsorbed by the substrate, the reactor walls and the target. There are two different modes. In the metallic mode, the target remains in a metallic state and the target voltage remains roughly the same. However, if more oxygen is injected the target can be poisoned and oxides form an insulating layer. This results in a sudden change in the voltage and a reduced deposition rate. For sputtering YSZ, where the secondary electron coefficient of ZrO_2 is higher than for the pure metal, the voltage will increase. By reducing the O_2 flow, the insulating oxides on the target are removed and the target returns to the metallic mode at a different flow rate than before, creating a hysteresis [23], [27].

2.1.4 Arcing

Arcs are a mechanism for collective electron emission from the cathode. A distinction is made between thermionic and cathodic arcs. At high temperatures, the most energetic electrons can overcome the potential barrier of the cathode surface and form an arc. Cathodic arcs, on the other hand, can also occur at room temperature. In this case, there is an explosive emission of electrons from a micrometer-sized hot cathodic spot. The material in the vicinity forms a completely ionized, rapidly spreading plasma. In addition, a liquid droplet is formed between the cold cathode and the dense plasma which is ejected from the cathode. This process should be avoided during sputter deposition.

The spots form due to thermal runaway. The electric field strength can be enhanced through geometric factors or charge build-up on insulating layers. A higher field strength leads to a higher electron emission which results in localized ohmic heating and an increase in temperature. A higher temperature increases the electron emission which leads to thermal runaway. This process forms a plasma and the spot is ignited. There a two different spot types. Type 2 spots occur on metal surfaces due to the geometric enhancement and type 1 spots emerge through nonmetallic layers. For reactive sputter depositions, the type 1 spots are especially a concern. During magnetron sputtering, there is always an area outside the racetrack, where an insulating layer forms which can lead to arcing [30]. The problem of arcing can be reduced by operating the deposition in the metallic mode.

2.1.5 Deposition Parameters for YSZ

Several parameters of the sputter deposition can be modified to obtain a dense columnar thin film.

One parameter is the substrate temperature. An increase in the substrate temperature enhances the mobility of the adatoms. This enables the adatoms to minimize the energy by moving to beneficial positions resulting in more densely grown thin films [20]. Lim et al. [31] showed that an increase in substrate temperature from room temperature to 500 °C increases the film density. However, for YSZ thin films an increase in temperature leads to an increase in grain size. This can restrict the efficiency of SOFCs due to fewer reaction sites at the electrolyte/electrode interface [31]. However, this could also be beneficial for oxygen ion batteries due to fewer grain boundaries resulting in a lower ionic resistance [32].

Another parameter is the atmosphere in the chamber. A lower pressure increases the mean free path of the sputtered atoms. Therefore they undergo fewer collisions and maintain more energy. This increases the mobility of the adatoms and promotes denser film growth. Furthermore, the destruction of the crystal growth by particles with high kinetic energy leads to denser growth as well due to the hindrance of continuous columnar crystal growth [20]. It was observed that at pressures of 0.59 Pa or 0.25 Pa the YSZ films exhibit a denser structure than at pressures of 4 Pa [33]. Hong et al. [34] observed a denser film growth with fewer pinholes when depositing the film at an Ar to O_2 ratio of 4:1 rather than a ratio of 13:1.

The positively charged ions are accelerated towards the substrate by applying a negative bias potential to the substrate. This can lead to denser film growth by providing energy to the adatoms and increasing their mobility. However, if the bias is too small the effect will be negligible and if the bias is too large the surface of the substrate will be sputtered as well as the target surface [25].

The applied power is especially interesting for the sputtering yield, the ratio between sputtered atoms to bombarding ions. At energies below the surface binding energy, there is almost no sputtering. Above a certain threshold, the ions have enough energy to lead to a collision cascade and eject surface atoms. The sputtering yield increases linearly with the ion energy until an ion energy of roughly 1 keV is reached where the behavior is nonlinear. If the energy is increased even further the sputtering yield decreases due to deep-ion implementation [35]. In YSZ reactive DC sputtering, the power applied to the target ranges from 1 - 17 W/cm^2, while the distance between the substrate and target varies between 5.5 - 7 cm [23], [25], [34]. For RF sputtering, the power applied to the target falls between 2.54 - 7.4 W/cm^2 [36]–[39].

2.2 Yttrium-Stabilized Zirconia

A typical crystal structure for fast oxide-ion conducting materials is a cubic fluorite type. Zirconia ZrO_2 is only present in this form at temperatures above 2300 °C. Figure 5 shows the crystal structure of fluorite-type zirconia.

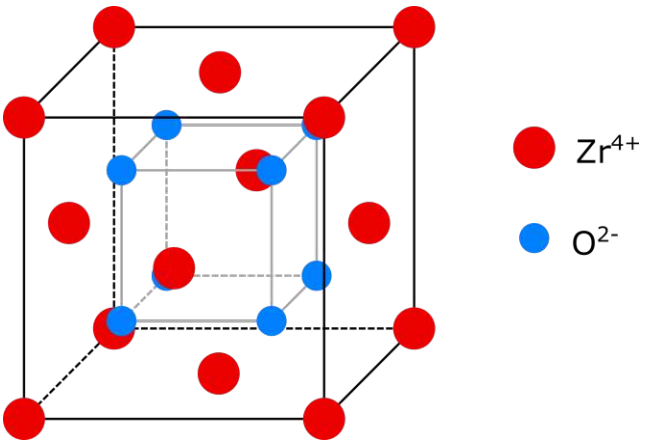

Figure 5: Fluorite crystal structure of ZrO_2 with red spheres Zr^{4+} an blue spheres O^{2-} [40].

However, by replacing sufficient Zr^{4+} ions with Y^{3+}, forming yttria-stabilized zirconia (YSZ), the cubic structure can be stabilized down to room temperature. In addition, the doping of the material generates oxygen vacancies which is important for the ion conduction over vacancy hopping [40]. However, the conductivity only increases until a doping concentration of about 8 mol% Y_2O_3 and then begins to decrease again. 8 mol% Y_2O_3 is also the amount of doping needed to stabilize the cubic phase [41]. The acceptor doping of zirconia with yttria is described by

$$Y_2O_3 + 2Zr_{Zr}^{\times} + O_O^{\times} \rightarrow 2Y'_{Zr} + V_O^{\bullet\bullet} + 2ZrO_2 \tag{3}$$

with the Kröger-Vink notation [40].

2.2.1 Ionic Conduction through Vacancies

The ionic conduction of YSZ is enabled by the diffusion of ions via vacancies. The ions are immobile and only when a vacancy of the same kind is close by they can leap into the vacancy. This process can be described by the movement of the vacancy instead of the ion which runs in opposite directions.

Figure 6 depicts the enthalpy against the position of an ion in an electric field. The enthalpy varies periodically with the position of the ion. Two stable lattice sites are separated by the distance a and the potential barrier h_0. In the graphic, the barrier to the right is reduced by

$$z_i e E \frac{a}{2} \tag{4}$$

with $z_i e$ the charge of the oxide ion, whereas to the left the barrier is increased by the same amount due to the electric field.

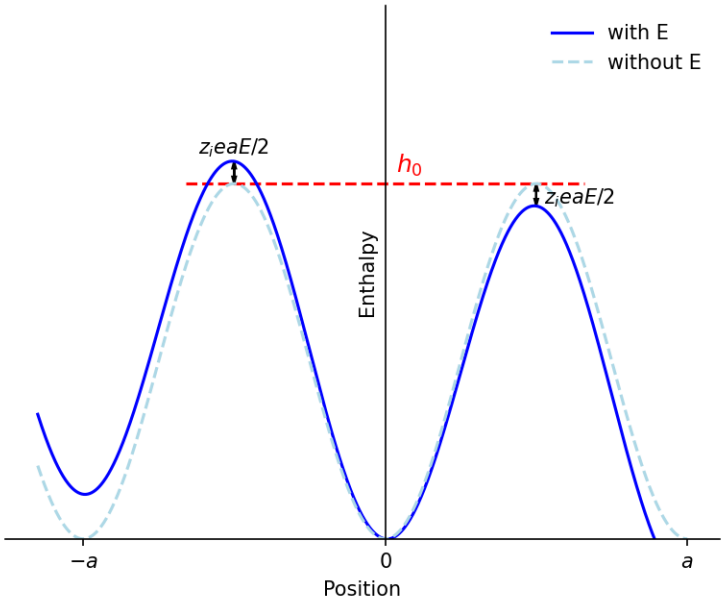

Figure 6: Enthalpy versus position of a charge carrier [42].

The electric current density of a species I_i in the left/right direction, without a concentration gradient, is calculated by

$$I_{i,left/right} = c_i z_i e a \nu_i e^{-\frac{h_0 \pm z_i eaE/2}{kT}} \tag{5}$$

with the concentration of a species c_i, the frequency of jump attempts over the barrier ν_i and the probability of success described by the Boltzmann factor. The net current is the difference between these two currents which results in

$$I_i = 2 c_i z_i e a \nu_i e^{-h_0/kt} \sinh \frac{z_i eaE}{2kT}. \tag{6}$$

In a small electric field, the sinh can be approximated by

$$\sinh x \approx x. \tag{7}$$

By combining equation 6 with equation 7 and comparing it $I_i = \sigma_i E$, the electric conductivity of a species σ_i in a small electric field is [42]

$$\sigma_i \approx \frac{z_i^2 e^2 c_i}{kT} a^2 \nu_i e^{-h_0/kT}. \tag{8}$$

2.2.2 Temperature Dependency of the Ionic Conductivity of YSZ

In [41] it was shown that the temperature dependency of the conductivity σ can be described by assuming that all vacancies are mobile and the average path of a vacancy contains two different types of barriers. YSZ acts like a series circuit of areas with two different resistivities. The temperature dependency of σ is expressed by

$$\sigma T = \left(\frac{1}{\gamma_1 e^{-E_{a,1}/kT}} + \frac{1}{\gamma_2 e^{-E_{a,2}/kT}}\right)^{-1} \tag{9}$$

with the two activation energies $E_{a,1}$ for the high and $E_{a,2}$ for the low barriers, the Boltzmann constant k, and

$$\gamma_i = \frac{z^2 e^2 a^2 n_{v,tot} \nu_i^0}{k\beta_i} \tag{10}$$

with the total vacancy concentration $n_{V,tot}$, the fraction of successful jumps over a barrier height β_i and a pre-factor ν_i^0 which includes the jump attempt frequency, a migration entropy term and correlation effects. The average path of a vacancy contains many more low barriers than high barriers because $\gamma_2 >> \gamma_1$. This leads to two different limiting cases due to the activation energies. At a high temperature, the jumping ions have sufficient energy to easily overcome the few high barriers and the activation energy depends on the lower barrier. However, at a low temperature, the activation energy is defined by the high barrier because the higher barriers get exponentially harder to pass [41]. Figure 7 shows a schematic of the two ionic conductivity regimes.

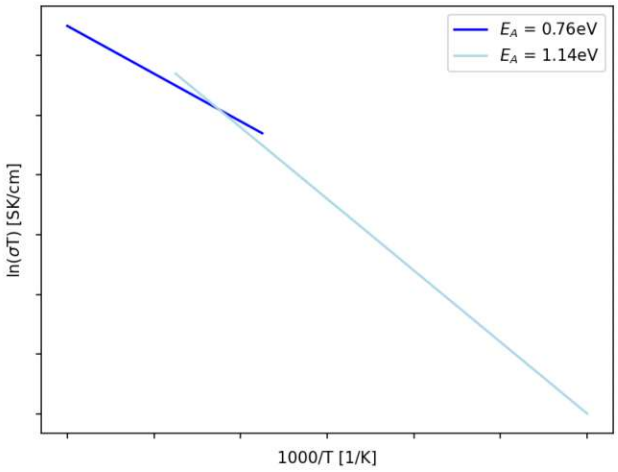

Figure 7: Schematic of the two ionic conductivity regimes of YSZ [41].

2.3 Electrochemical Impedance Measurement

Electrochemical Impedance Spectroscopy (EIS) measurements are performed by applying a small sinusoidal voltage with different frequencies f and measuring the sinusoidal current response. By comparing the ratio between the voltage and the current and the phase shift at different f, the impedance $Z(f)$ of the measured system can be calculated [43]. A common way to illustrate the data of EIS is Nyquist plots. In these plots, the imaginary part of Z is plotted vs the real part of Z.

Electrical equivalent circuits, consisting of resistors R, inductors L and capacitors C, are used to analyze the EIS spectra. The electrical properties of the sample can be modelled with a combination (series or parallel) of these elements with the respective impedances:

$$Z_R = R \tag{11}$$

the impedance of an inductor

$$Z_L = j2\pi fL \tag{12}$$

and the impedance of a capacitor

$$Z_C = \frac{1}{j2\pi fC} \tag{13}$$

through fitting the data with a suitable equivalent circuit. However, the capacity is often nonideal. Therefore constant phase elements with impedance

$$Z = \frac{1}{C(j2\pi f)^{\alpha}} \tag{14}$$

can be used, where α takes into account that the measured spectra often exhibit a nonideal C. An $\alpha = 1$ describes an ideal capacitor [44].

3 Experimental

3.1 Sputtering Device

In Figure 8 a picture of the sputtering device with the main components is shown. The base of the device is a spherical vacuum chamber with different flanges. The machine is equipped with a Gencoa sputtering gun (model number: SW50-3G(A)-WMF) with a circular balanced magnetron for targets with a diameter of 5.08 cm and a shutter. The gun can be supplied with power from two different sources. An RF-generator with a frequency of 13.56 MHz from Seren (model number: R301 300W, 13.56 MHz RF Generator) for RF-sputtering and a DC power source from Pervac (model: M600DC-PS) to enable reactive DC-sputtering.

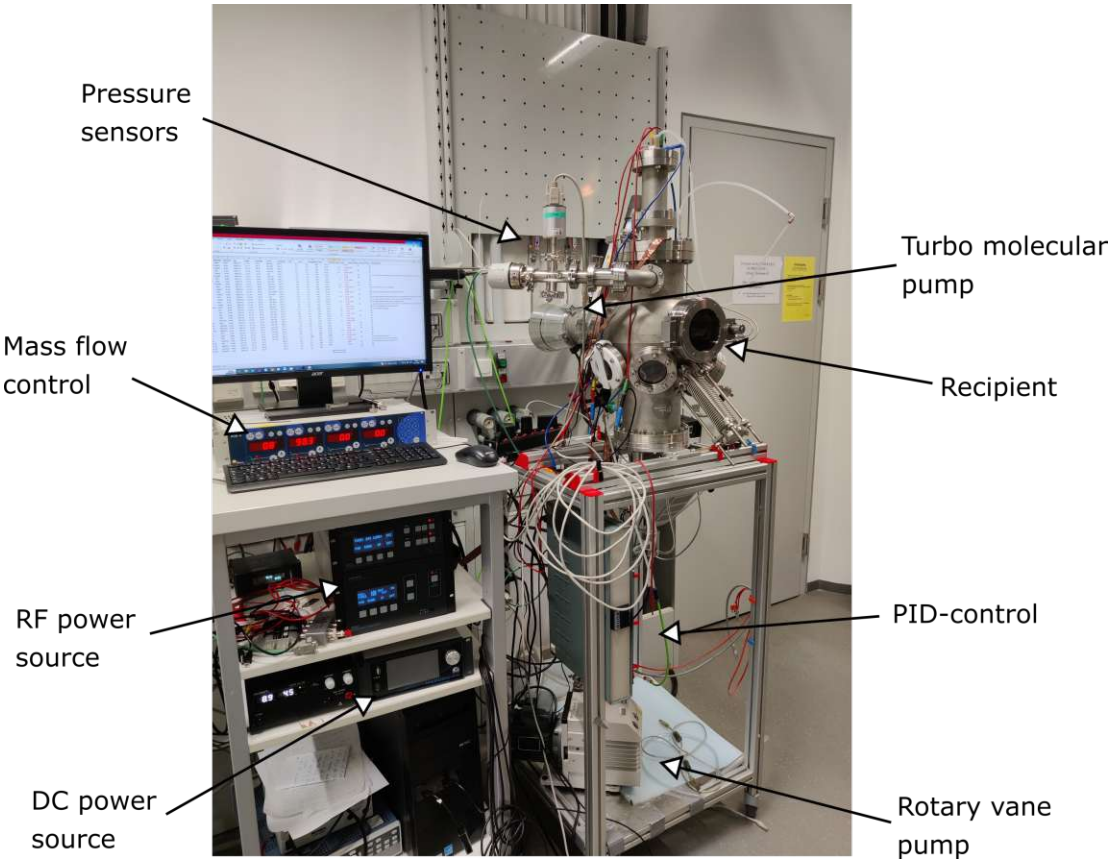

Figure 8: Picture of the sputtering device with the main components.

The device is also equipped with a rotary vane pump and a turbo molecular pump for the generation of a vacuum. The reachable base pressure is $\approx 1.5 \times 10^{-5}$ mbar. A mass flow controller is used to separately control the flow of Ar and O_2. The chamber has two different gas inlets. One inlet via the sputtering gun for Ar or a combination of Ar and O_2 and a second inlet for O_2 close to the substrate to prevent target poisoning. A valve in front of the turbo molecular pump is used to control the pressure inside the chamber. In order to measure the pressure inside the chamber, it is equipped with two pressure sensors. An MPG400 sensor from Inficon for a large pressure range and a retrofitted CTR100 sensor from Leybold for a more accurate measurement of the pressure during the deposition.

The sample stage is equipped with a heater and eight separate electrical contacts for a thermocouple, in-situ measurements and to apply bias. The sample stage also holds the sample holder of stainless steel with a hole in the middle with a diameter of 25 mm. It can be fitted with different ceramic masks for different substrate sizes which are pinned down by springs. Next to the sample stage is a quartz scale to measure the deposited film thickness. For cooling the sputter device has a water cooling cycle which is connected to the gun, the sample stage and the quartz scale. The temperature of the heater is measured by a thermocouple and can be controlled via a proportional–integral–derivative controller.

Two different configurations of the chamber were tested. In one configuration the target was at the top and the substrate holder was at the bottom. In the other configuration, it was sputtered from bottom to top to prevent dirt particles from dropping onto the substrate. Additionally, the device is equipped with cables for the grounding of the chamber. This is especially important during RF-sputtering. For a good RF shielding electrical conductors with a big surface are used. In particular, the electric connection between the top of the gun and the ground is important to avoid electrical interference of the other devices. Figure 9 shows the inside of the vacuum chamber and the main components.

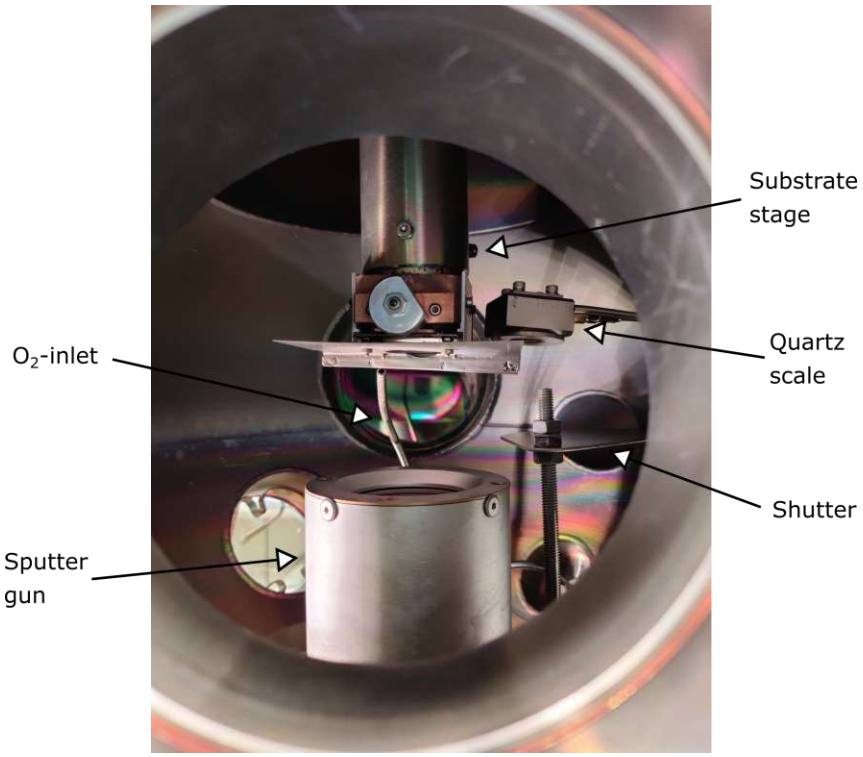

Figure 9: Inside of the vacuum chamber with the main components.

Two different YSZ targets are available for the device. A metallic ZrY target with 15 wt% Y, a diameter of 5.08 cm, a thickness of 3 mm and a purity auf 99.9 % from MSE Supplies. A picture of this target is shown in Figure 3. The other target is a ceramic YSZ target with a ratio of ZrO_2 to Y_2O_3 of 92 to 8 mol%, a diameter of 5.08 cm, a thickness of 3.18 mm and a purity of 99.99 % from Advanced Engineering Materials.

3.2 Sample Preparation - Sputter Process

3.2.1 Test Sample Structure

The main goal of this sample setup is detecting pinholes and enabling measurements of the film thickness. Figure 10 illustrates the sample setup. For the first few samples, quartz disks with a diameter of 25 mm were used. However, for most of the samples, the substrate was a single crystal with the size 10x10 mm^2 of either YSZ, Si or strontium titanate. The first layer is 100 nm of DC-sputtered Pt at a pressure of 2 Pa and a current of 100 mA. These parameters are used for every Pt layer. The layer is either sputtered at room temperature or at about 700 °C substrate temperature. When the Pt layer is cold-sputtered, an additional interlayer of 5 nm Ti at a pressure of 0.73 Pa and 100 mA is deposited to increase adhesion between the substrate and the Pt layer. For the hot deposition, the heater set temperature is 1000 °C which leads to approximately 700 °C substrate temperature. The next layer is either an RF or DC-sputtered YSZ thin film with varying plasma power, pressure, O_2 to Ar ratio, bias, substrate target distance and substrate temperature. These parameters will be discussed in more detail in chapter 4.

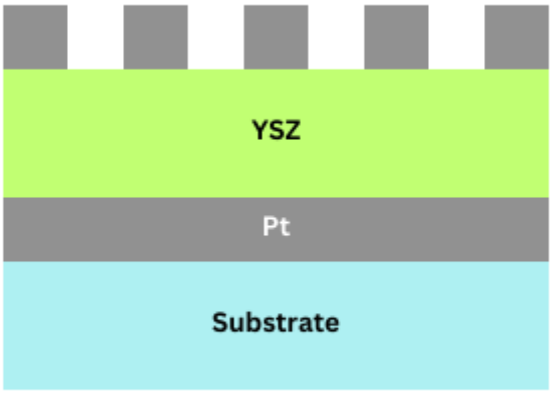

Figure 10: Sample structure.

During the deposition, either ZrO_2 paste or a mask is used to prevent film growth in certain areas to enable electric contact with the Pt layer and to measure the thin film thickness. If ZrO_2 paste was used the paste was removed with ethanol and a cleanroom wipe. The last layer is cold-sputtered Pt microelectrodes with a thickness of 100 nm and a 5 nm Ti interlayer. To create the microelectrodes, a 3D-printed mask of ABS is used. The mask has holes with a diameter of 0.6 mm with 1.4 mm between them. However, the generated microelectrodes are not perfectly circular and are of different sizes due to the imperfection of the mask. If the thin film seemed to be electrical insulating, a large Pt macroelectrode with a Ti interlayer with the same deposition parameters as the microelectrodes were used instead of microelectrodes.

3.2.2 Oxygen Ion Battery Structure

After generating dense YSZ thin films an oxygen battery was constructed. A sketch of the sample setup is displayed in Figure 11. It consists of a 10x10 mm^2 YSZ single crystal as substrate. A 100 nm Pt mesh, serving as a current collector, is sputtered and structured by photo-lithography and ion beam etching on both sides of the sample. On the bottom side, a 500 nm layer of porous $La_{0.6}Sr_{0.4}CoO_{3-\delta}$ (LSC) is grown on top of the current collector by pulsed laser deposition (PLD). The other side is covered by a 400 nm thin film of $La_{0.6}Sr_{0.4}FeO_{3-\delta}$ (LSF) via PLD serving as an electrode. Then two YSZ thin films were DC-sputtered onto this layer generating an electronically insulating and 814 nm thick thin film. Then a 400 nm $La_{0.5}Sr_{0.5}Cr_{0.2}Mn_{0.8}O_{3-\delta}$ (LSCrMn) layer was deposited by PLD onto the sample as the other electrode. At last, a 100 nm Pt layer was sputtered. Then the electrodes were closed gas-tight by brushing glass on the sample and subsequently sintering the sample for 2 h at 750 °C. For an electric contact with the electrodes, the Pt layers on the top side of the sample have bridges to the edge of the substrate. Table 1 summarizes the deposition parameters.

Table 1: Depositing parameters of the thin films.

	LSF	LSCrMn	LSC (porous)	YSZ	
Method	PLD	PLD	PLD	DC-sput.	
Laser pulses	43	31	25	-	[nm^{-1}]
Laser fluence	1.1	1.1	1.4	-	[J cm^2]
Pulse frequency	10	10	5	-	[Hz]
O_2 pressure	4	1.5	5	0.15	[Pa]
Ar pressure	-	-	-	0.3	[Pa]
Current	-	-	-	500	[mA]
Target to substrate Distance	6	6	6	5	[cm]
Substrate Temperature	600	700	450	600	[°C]

Figure 11: Sample set up of the oxygen battery.

3.2.3 Quarz Scale

The chamber is equipped with a quartz scale to monitor the deposition rates and the resulting film thickness. During some depositions, this was not possible due to electrical interference with the quartz balance caused by the RF plasma and shading of the quartz scale through some substrate holder setups.

Figure 12 shows an example of the resonance frequency plotted against the time of DC-sputtering deposition of sample YSZ_25. This behavior is representative of most of the depositions where it was possible to read out the resonance frequency. The slope is constant, which indicates a constant deposition rate.

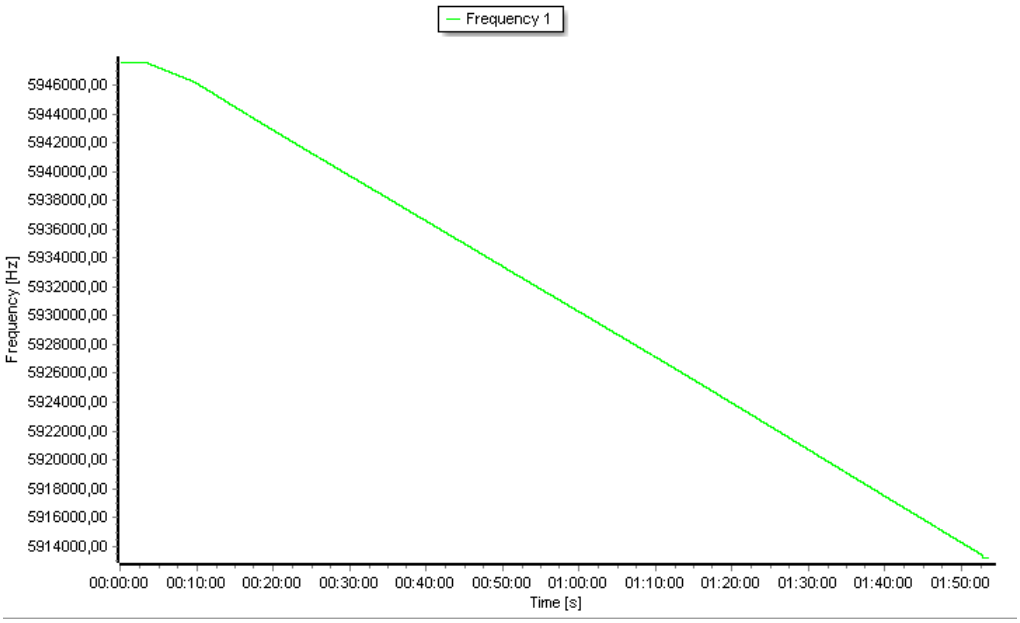

Figure 12: Resonance frequency vs time of sample YSZ_25.

The sample thickness was later evaluated via profilometer and SEM cross-section measurements and compared to the resonance frequency change of the quartz scale to evaluate the frequency change per nm. The profilometer and SEM measurements were in good agreement and resulted in approximately 40 Hz change of the frequency per nm film grown on the substrate.

3.2.4 Substrate Temperature

During the deposition, only the heater temperature was tracked with a thermocouple. Therefore, the sample temperature was estimated by heating samples with known emissivity to deposition conditions and measuring their temperatures via an infrared pyrometer. One sample was a YSZ single crystal with a sputtered Pt layer on the side facing the heater, the other one was a YSZ single crystal with a brushed lanthanum strontium cobalt ferrite (LSCF) layer. These two samples were measured with a slightly different sample holder setup which possibly leads to differences due to a different substrate heater distance. Figure 13 shows the measured substrate temperature against the corresponding heater temperature. The sample with the mixed conductor has a consistent offset of

about 200 °C compared to the heater temperature whereas the probe with Pt has a lower offset at lower temperatures which increases with increasing heater temperature.

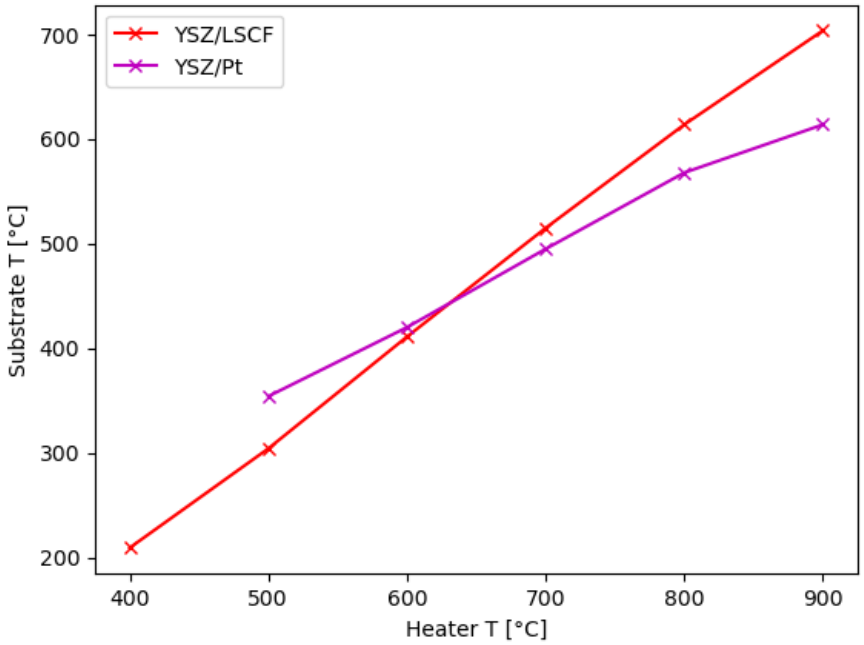

Figure 13: Substrate temperature vs heater temperature of a YSZ single crystal with either a layer Pt or LSCF

It should be noted that the actual substrate temperature during deposition may be slightly different due to different sample setups and the additional heating due to the sputtering deposition. The two measured samples were chosen to be as close to the actual sample setups as possible and still have a surface of the YSZ single crystal facing the pyrometer.

Furthermore, the substrate temperature (measured by pyrometer) showed a better correlation with the heater power than with the heater PID setpoint. In Figure 14 the set temperature and the power are plotted against the substrate temperature. The curves for the power are similar whereas the heater set temperature and substrate temperature have an offset between the different measurements. Therefore the power is a better indicator of the substrate temperature than the thermocouple.

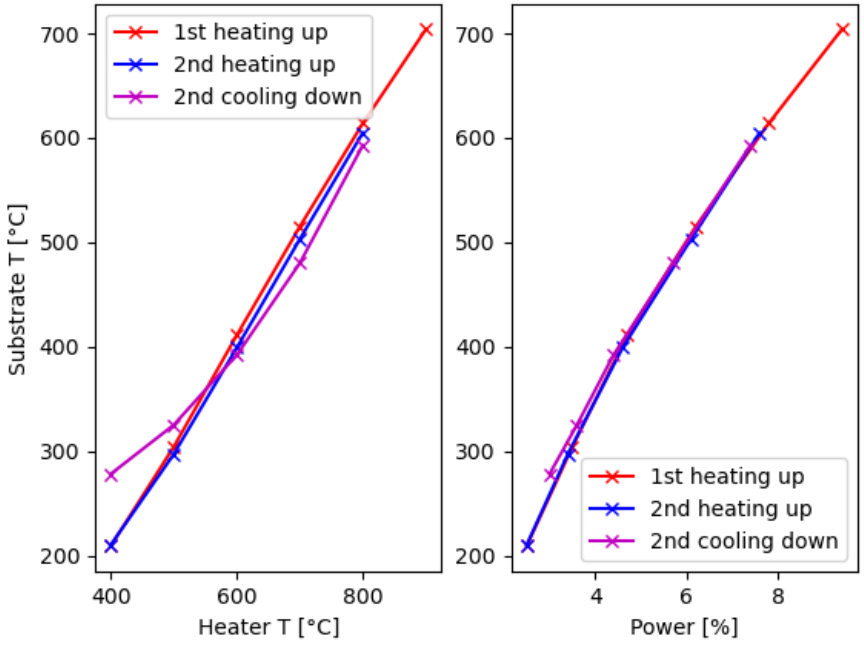

Figure 14: The heater set temperature and the power vs the substrate temperature of the YSZ sample with LSCF.

3.3 Characterization Techniques

Various measurements are carried out to analyze the thin films. The main focus was on electrochemical measurements via EIS. The composition of the thin films was measured by X-ray fluorescence spectroscopy (XRF) and by laser-induced breakdown spectroscopy (LIBS). For structural characterization scanning electron microscopy (SEM) of the surfaces and cross-sections were performed. In addition, one sample was measured via grazing incidence X-ray diffraction. Also, stylus profilometer scans with a DekTak XT (Bruker) with the analysis software Vision64 were conducted to evaluate the film thickness. The samples were also regularly inspected with a light microscope.

3.3.1 Pinhole Detection

If the sputtered YSZ thin film contains pinholes or other imperfections, there is an electrical contact between the microelectrodes and the Pt layer below the YSZ. EIS is performed to detect the pinholes. At room temperature, the YSZ layer is insulating and if a low resistance between the microelectrode and the Pt layer is measured the thin film contains pinholes. Figure 15 shows the different cases of EIS data at room temperature. The measurement data of plot (a) belongs to two microelectrodes with large pinholes. The bigger the pinhole the smaller the electrical resistance. (b) shows the data of a microelectrode with a small pinhole. Plot (c) displays the measurement of either a very small pinhole or some residual conductivity and (d) shows the desired behavior of an electrical insulating microelectrode.

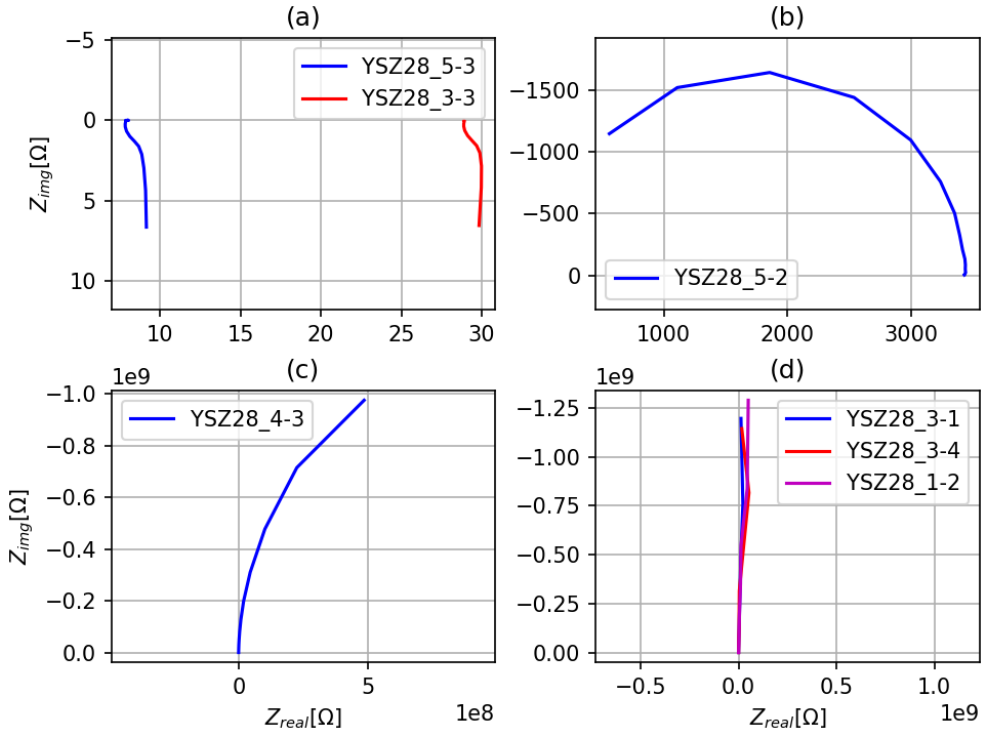

Figure 15: EIS data of different microelectrodes at room temperature. (a) examples for a large pinhole, (b) example for a small pinhole, (c) very small pinhole/residual conductivity and (d) electrical dense measurements.

3.3.2 Electrochemical Characterization of the Test Samples

Impedance spectroscopy was performed with an Alpha-A High Performance Frequency Analyzer (Novocontrol). The measurement setup for the samples with microelectrodes consisted of a light microscope, an asymmetric heater onto which the samples were placed and two micromanipulators with Pt needles. The needles were used to contact one microelectrode and the Pt beneath the YSZ layer to enable a cross-plane impedance measurement. For the pinhole detection, the samples were measured at room temperature in ambient air over a frequency range from 10^6 MHz to 1 Hz with a resolution of 5 points per decade and an output voltage of 0.1 V. Some of the electrically dense microelectrodes were also measured at different temperatures. The heater set temperatures were between 150 to 600 °C resulting in approximately 100 to 550 °C and were varied in 25 °C steps. Due to the asymmetric setup, the sample temperature had an offset to the heater temperature. The samples were measured at least once with an increasing temperature and at least once with a decreasing temperature to observe if the thin film was altered by the heat treatment. Furthermore, the output voltage was changed to 0.05 V with a higher integration time and a higher resolution with 10 points per frequency decade.

A different measurement setup was used for measuring the temperature dependency of the ionic conductivity of the electronically insulating thin films in between two Pt electrodes. These samples were placed in a symmetric heater with a thermocouple close by, to measure the actual temperature of the sample. The other measurement parameters stayed the same.

3.3.3 Electrochemical Characterization of the Oxygen Ion Battery

The sample was placed in a symmetric heater configuration at a temperature of 350 °C, measured by a thermocouple, and at an O_2 partial pressure of 0.25 mbar for the electrochemical characterization of the battery. The electrical contact to the LSC layer was established by placing the sample on a Pt sheet. The electrodes were contacted at the Pt bridges with Pt needles. Before the measurements, the sample was equilibrated with the atmosphere to ensure a defined oxidation state of the electrodes. This was achieved by short-circuiting the electrodes with the bottom LSC layer. A current between 10 to 1000 µA was pumped between the electrodes. The sample was cycled multiple times by changing the current direction until a certain upper or lower cell voltage was reached. During the cycling, the cell voltage between the LSF and the LSCrMn electrode and the potential of LSF to the atmosphere was measured. This was conducted with a Keithly 2600 source meter in a galvanostatic mode in a 4-wire configuration.

4 Results

4.1 Sputter Process

4.1.1 RF-Sputtering

In the following section, the RF-sputtered thin films and the effect of the different parameters will be discussed. Table 2 lists the RF-sputtering depositions and some of the important parameters. All RF-sputtered samples were deposited from top to bottom. In addition during the deposition of YSZ_3, 10, 11 and 18 a bias of −30 V was applied to the target. These were the only samples with bias, which was also rather low, because as soon as the bias was increased, further electric flashovers occurred on the sample stage. The sample stage was not adapted to enable a larger bias. In the testing, YSZ_17 and YSZ_18 were compared and the only difference between those two probes was the use of bias in YSZ_18. However, testing showed that YSZ_17 had a higher percentage of dense microelectrodes. Therefore, it did not seem necessary to use bias to achieve a dense thin film.

Table 2: RF-sputtering parameters.

sample	temperature heater [°C]	pressure [Pa]	power [W]	time [min]	Ar/O_2	thickness [nm]	dense microele.
substrate target distance approx. 8 cm							
YSZ_1	0	0.33	80	120	1/3	-	0/8
YSZ_2	800	0.33	80	240	1/3	130	0/18
YSZ_3	800	0.38	80	300	1/3	170	0/10
YSZ_4	800	0.65	80	240	1/3	90	0/7
YSZ_6	800	0.345	80	240	1/5	170	0/10
YSZ_9	800	0.345	90	240	1/5	220-300	0/17
YSZ_11	900-800	0.344	100	240	1/5	200	0/8
YSZ_12	700	0.340	100	240	1/5	190	4/12
substrate target distance approx. 6 cm							
YSZ_13	900	0.341	80	240	1/5	192	0/12
YSZ_14	900	0.341	100	240	1/5	295	4/20
YSZ_15	800	0.23	100	240	1/5	345	3/21
YSZ_16	800	0.326	100	240	1/3	290	0/20
YSZ_17	800	0.334	100	210	1/5	240	4/18
YSZ_18	800	0.334	100	240	1/5	280	2/20
YSZ_19	800	0.341	125	240	1/5	620	19/20
YSZ_20	800	0.341	125	240	1/5	420	-
YSZ_21	800	0.333	150	240	1/5	520	13/18
YSZ_22	800	0.451	130	240	1/4	430	17/23
YSZ_23	850	0.295	130	240	1/4	440	18/24
YSZ_24	850	0.4	140	300	1/10	766	17/22

An increase in pressure during the deposition leads to a decrease in deposition rate, which is most likely due to an increase in collisions on the path to the substrate. This trend is derived by comparing YSZ_2 to YSZ_4 and YSZ_14 to YSZ_15. In both cases, the major difference is the pressure. However, a lower pressure leads to a higher film thickness, but not necessarily to a higher amount of dense microelectrodes.

Another important parameter is the power applied to the target. A higher power results in a higher deposition rate. Furthermore by comparing YSZ_18 to YSZ_19, the increase in power leads to a drastic increase of insulating microelectrodes. This is possibly due to a higher film thickness or a higher mobility of the adatoms. Furthermore, a reduction in the target to substrate distance ensued in an increase of film thickness and amount of electrically insulating microelectrodes (comparison YSZ_12 to YSZ_14).

Parameters for a desired dense film growth are a power between 130 - 150 W, a pressure between 0.291 - 0.451 Pa, a ratio of Ar to O_2 of 1/5 or 1/4 and a heater set temperature of around 800 °C. These parameters were used for YSZ_21 to YSZ_23. These samples have approximately 75 % of dense microelectrodes. The remaining pinholes are most likely due to dust particles preventing the YSZ film growth in certain areas. This problem will be discussed in chapter 4.1.3.

In addition, one RF-sputtered sample was deposited with the ceramic target. Therefore less O_2 is needed for the sputtering process because the target is already the desired compound. The parameters in table 2 for YSZ_24 lead to the desired dense film growth with 77.3% dense electrodes. However, dirt particles most likely generated pinholes. Figure 16 is a picture of a pinhole of YSZ_25 generated through the shading of a dirt particle.

Figure 16: Pinhole due to a dirt particle of YSZ_25.

4.1.2 DC-Sputtering

It was also tested to produce thin films via reactive DC-sputtering due to a faster deposition rate and fewer grounding issues. Table 3 lists the main parameters of some reactive DC-sputtered samples, which were sputtered from top to bottom.

Table 3: DC-sputtering parameters.

sample	temperature heater [°C]	pressure [Pa]	power [W]	time [min]	O_2/Ar	thickness [nm]	dense microele.
YSZ_25	800	0.5	200	120	1/4	826	15/20
substrate target distance approx. 5 cm							
YSZ_26	800	0.5	200	120	1/4	673	4/20
YSZ_27	800	0.5	160	120	1/6	678	5/20
YSZ_28	600	0.5	≈145	120	1/3	460	16/23

YSZ_26 and YSZ_27 had a lower deposition rate and fewer dense microelectrodes than YSZ_25 even though the deposition parameters were similar. During the preparation of these two samples, a lot of arcing occurred due to O_2 inlet close to the substrate. The similar film thickness of YSZ_26 and YSZ_27 indicates that the target poisoning reduced the deposition rate because YSZ_27 was deposited with less power and lower O_2 partial pressure.

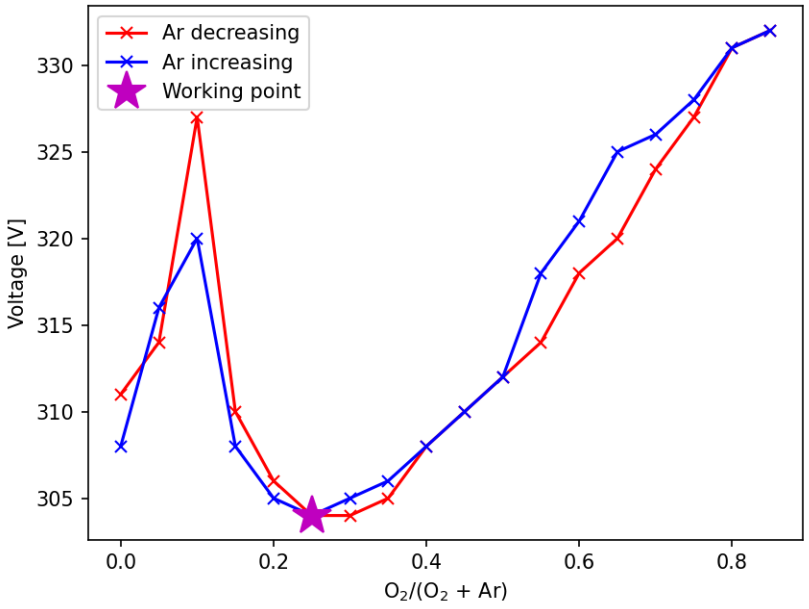

Figure 17: Measured posing curve with 500 mA and a pressure of 0.5 Pa.

Furthermore, another setup was investigated with the chamber rotated by 180° to reduce dirt particles on the substrate surface and an O_2 inlet close to the substrate surface to reduce target poisoning and enable a higher O_2 flux. To find a suitable operating point

for the deposition, a poisoning curve was recorded. This was performed with a constant current to the target of 500 mA and a pressure of 0.5 Pa. The Ar to O_2 ratio was changed step by step while leaving the sum of the flow of both gases constant. At every ratio, the voltage needed for the 500 mA current was recorded. Figure 17 shows the measured poisoning curve. The curve does not show the expected hysteresis of the curve between increasing and decreasing Ar content. However, after the ratio of 0.25, the voltage needed increases, which indicates the region where the target is poisoned. Therefore, the ratio of O_2 to Ar of 1/3 was chosen as the operating point where the target is still in the metallic mode. The initial spike at 0.1 on the curve is unclear, and conducting additional measurements might provide clarification.

The deposition with the working point of the poisoning curve still had a significant amount of arcing with even 19 arcs per minute, but the sample YSZ_28 had 69% of dense microelectrodes and a film thickness of 460 nm with a power of about 146 W. This issue occurred probably due to insufficient pre-sputtering and residual remains of oxides on the target surface. This was resolved through pre-sputtering, reducing the amount of arcing to less than three arcs per minute at this working point.

Furthermore, during some deposition, an unusual amount of arcing occurred in the middle of the target. This was most likely due to geometric effects or target poising. Therefore, the target was grinded down, which resolved the issue. As a result, arcing was reduced from over 15 arcs per minute to less than three.

4.1.3 Dirt Particles

A significant issue when aiming at dense thin films is the formation of pinholes caused by dirt particles, as depicted in Figure 16. To investigate the origin of the particles the sample YSZ_30 was investigated after every work step under the light microscope. To ensure a clean substrate a new cleaning procedure was used instead of ethanol and a cleanroom wipe. The silicon single crystal underwent a cleaning process involving two cycles in an ultrasonic bath with Extran, followed by one cycle in double-distilled water, and another in ethanol, each lasting 15 minutes. Figure 18 shows the cleaned substrate. However, it should be mentioned that there are still some remaining particles that can not be prevented outside of a clean room. Furthermore, in the right corner, you can still see some residuals of the ethanol.

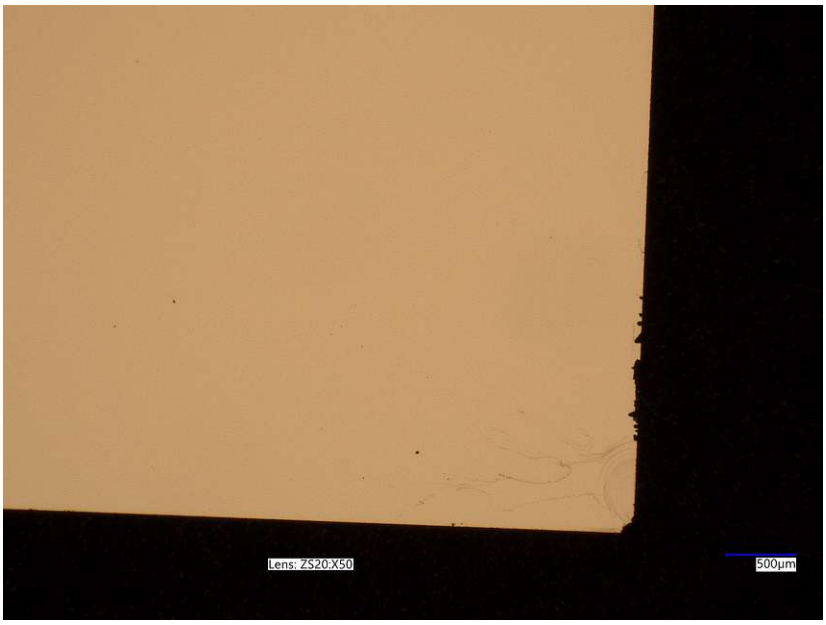

Figure 18: Cleaned Si substrate.

In the next step 5 nm Ti and the 100 nm Pt were sputtered onto the substrate. This thin film is afterwards cleaned with ethanol and removing the ethanol with a flow of N_2. The resulting surface is displayed in Figure 19. The amount of particles on the surface increased compared to the single crystal and it was not possible to remove all the particles.

Figure 19: Cleaned Pt surface.

Afterward a YSZ layer was sputtered onto this surface for 2 h with the deposition parameters in table 4.

Table 4: DC-sputtering parameters of two times deposited samples.

sample	temperature heater [°C]	pressure [Pa]	current [mA]	O_2 flow [sccm]	Ar flow [sccm]	heating/cooling rate [°C/min]
YSZ_30	600	0.45	500	2.5	7.5	30/15
YSZ_33-YSZ_37	800	0.45	500	2.5	7.5	30/15

Figure 20 shows the uncleaned surface of the deposited YSZ layer. There are two large particles visible with one over 50 µm in length. These particles do not originate from the transport of the sample through the air but stem from inside the sputtering chamber. Even though it is sputtered from bottom to top large particles can end up on the sample.

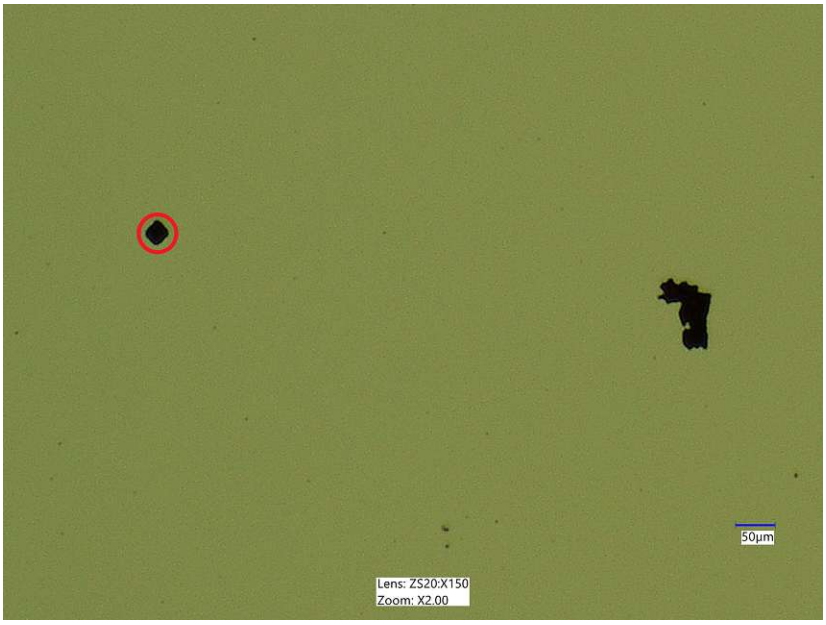

Figure 20: Sputtered YSZ layer uncleaned.

After cleaning with ethanol and an N_2 flow the large particles are removed. The particle marked in Figure 20 is gone but an area with no YSZ layer remains which can be seen in Figure 21. However, Figure 22 demonstrates that with this cleaning procedure, not all of the dirt is removed.

Figure 21: Cleaned YSZ surface with pinhole.

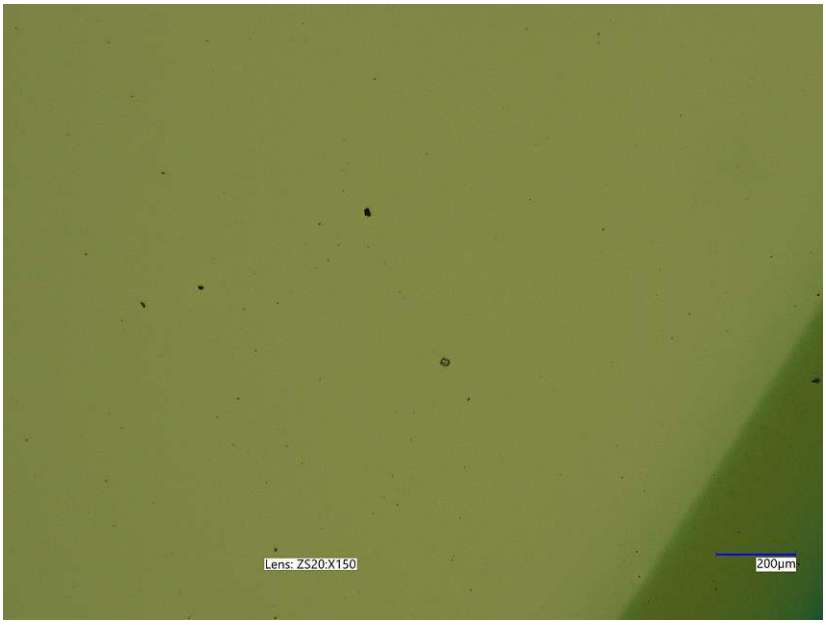

Figure 22: Cleaned YSZ surface with remaining dirt particles.

To close the pinholes that are generated through the shading of particles another YSZ layer was sputtered onto the same sample with equal deposition parameters for 2 h. However, during pre-sputtering parts of the YSZ layer sputtered onto the shutter detached and dropped onto the target. Figure 23 shows the uncleaned surface of the second layer. The second layer is obviously more contaminated by dirt than the first layer and the only difference was the particles that dropped onto the target. Therefore, it is assumed that dirt particles that fall onto the target are flung onto the substrate and hinder film growth.

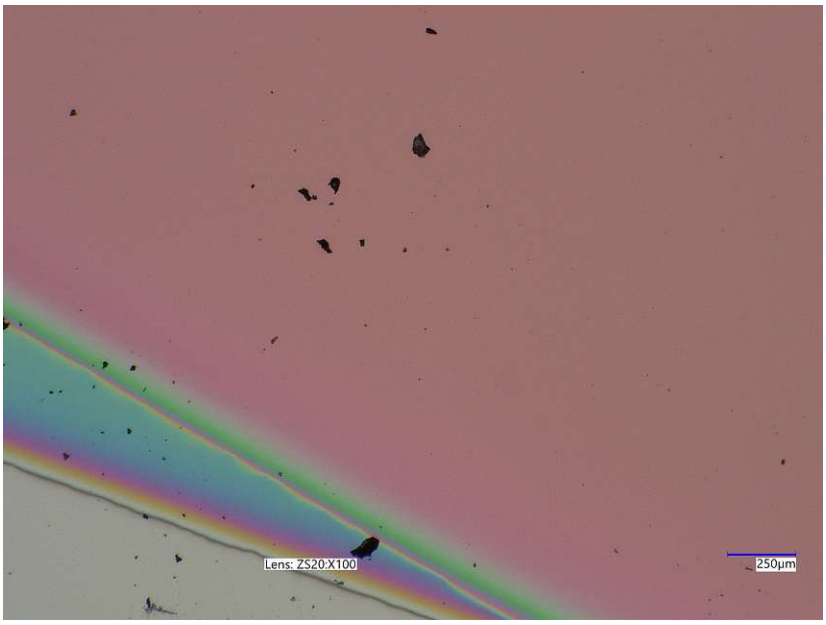

Figure 23: 2nd YSZ layer.

Subsequently, the sample underwent cleaning and was reexamined using a light microscope. In Figure 24, the previously concealed pinhole from Figure 21 is now apparent.

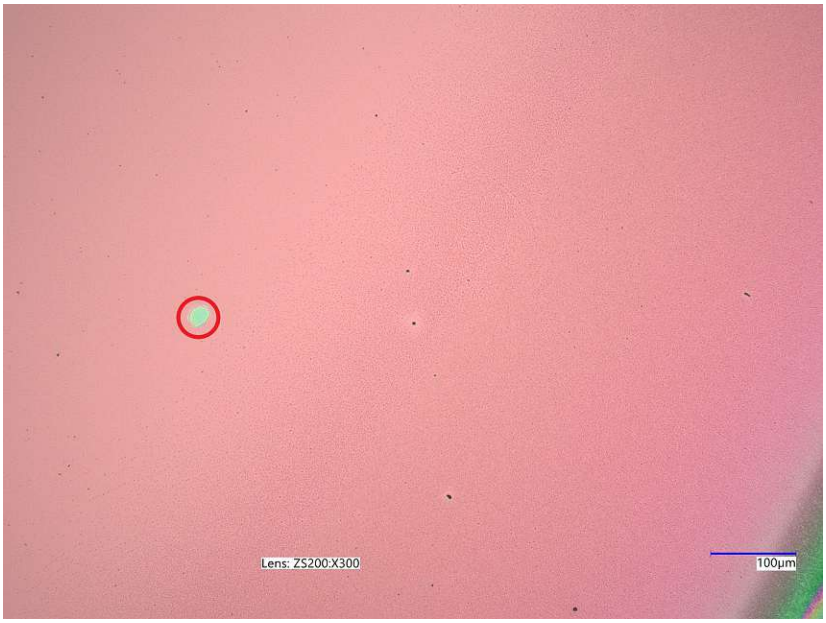

Figure 24: Covered pinhole by the 2nd YSZ layer.

Then microelectrodes were sputtered onto YSZ_30 and measured via EIS. The new cleaning procedure and the deposition of two thin films resulted in 90.5% electrical dense microelectrodes. Figure 25 indicates that pinholes of the first depositions are indeed covered up and are electrically dense. However, Figure 26 of a microelectrode with a short circuit shows that possibly not all pinholes are closed successfully. This is most likely due to insufficient cleaning before the depositions of the YSZ thin films and the high amount of dirt particles inside the chamber. Therefore the chamber was cleaned via sandblasting to reduce dirt particles inside the chamber and the cleaning procedure was adapted with additional wiping of the sample with a clean room wipe.

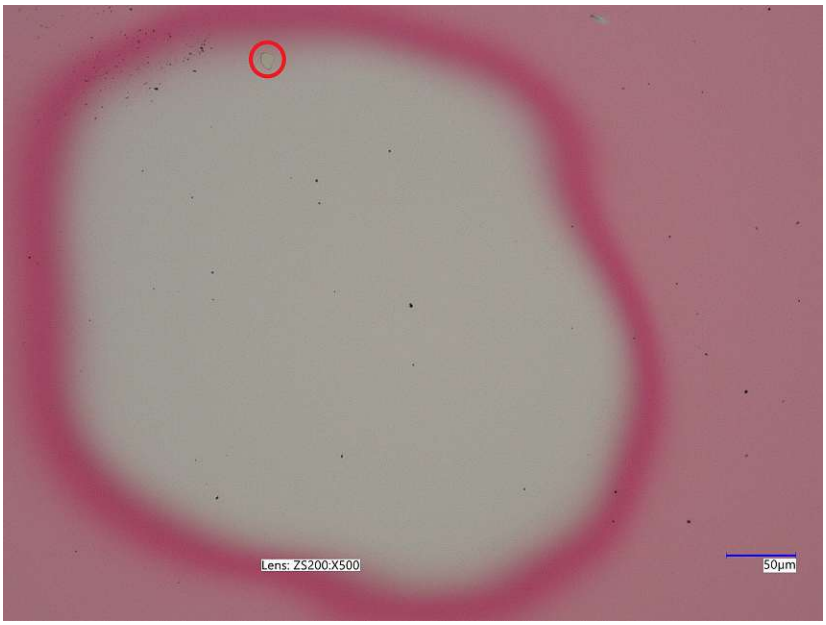

Figure 25: Electrically dense microelectrode with covered-up pinhole.

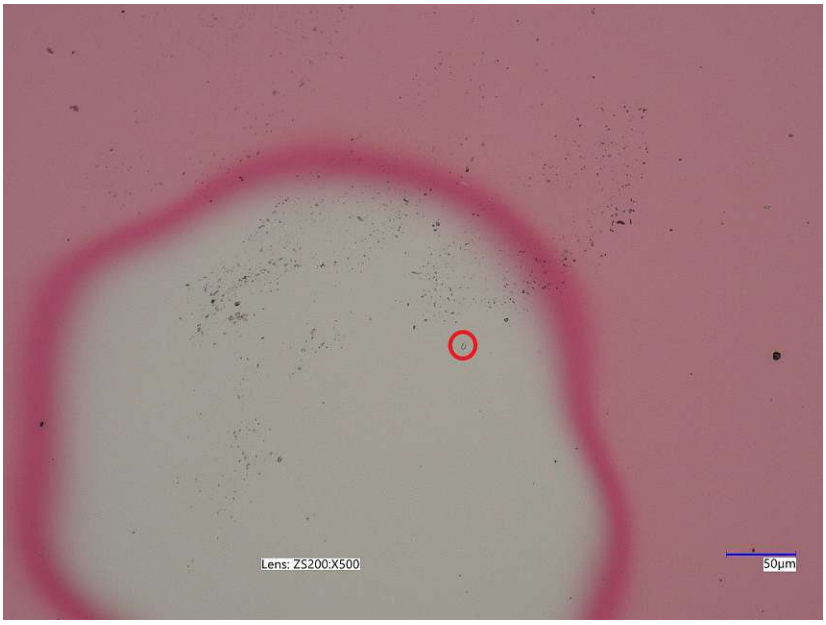

Figure 26: Microelectrode of YSZ_30 with a short circuit. The area with the possible pinhole is marked with a red circle.

4.1.4 Final Procedure

The final procedure for electrically dense thin films will be explained based on the first dense sample YSZ_33. Onto this sample, YSZ was sputtered twice with the same parameters as in table 4 except for the heater set temperature which was increased to 800 °C. At first, the chamber has to be cleaned. For this, the shutter, the containment ring of the gun and the shielding of the substrate holder is cleaned via sandblasting. Additionally, the vacuum chamber is evacuated out to reduce the amount of dirt particles.

When the chamber is cleaned, the same atmosphere as for the deposition is created without the sample inside the chamber. This is for pre-sputtering and conditioning of the target for the deposition. At first, the current to the gun is set to 300 mA and then it is slowly ramped up to 500 mA. The target is cleaned until the applied voltage to the target is stable. Then the sample is cleaned with ethanol a clean room wipe and a N_2 flow and placed inside the chamber. During the heating process the temperature is increased by 30 °C/min and the chamber is pumped down to a pressure of around 1.7×10^{-3} Pa. As soon as this pressure and the temperature are reached the gases are let into the chamber and the atmosphere is adjusted to the desired pressure.

Again the target is pre-sputtered with 500 mA, but with a closed shutter until the applied voltage is stable. This can take up to 10 min. Once the voltage is stable the shutter is opened and the deposition begins. After 2 h the plasma is turned off and the heater is cooled down at a rate of 15 °C/min. When the heater is cold the gases are turned off and the sample can be taken out of the chamber.

Then the chamber is cleaned again. Especially the containment ring of the gun needs to be sandblasted. The sample is then cleaned with ethanol, a cleanroom wipe and a N_2 flow again to remove the particles that landed on the sample during the first deposition. If the target was not used for some days it needs to be pre-sputtered again without the sample. Other than that the procedure is the same as before to close the pinholes of the first deposition. This procedure resulted in a completely electrical dense YSZ thin film of 814 nm.

4.1.5 Remaining Problems

Even though parts of the chamber are regularly sandblasted there are still concerns about particles dropping from the containment ring onto the target and therefore possibly contaminating the sample. Figure 27 is a picture of the containment ring after a 2 h long deposition. During this time a crumbly layer developed which partially peels off the containment ring and drops onto the target. This issue cannot be solved by sandblasting because this layer forms too quickly.

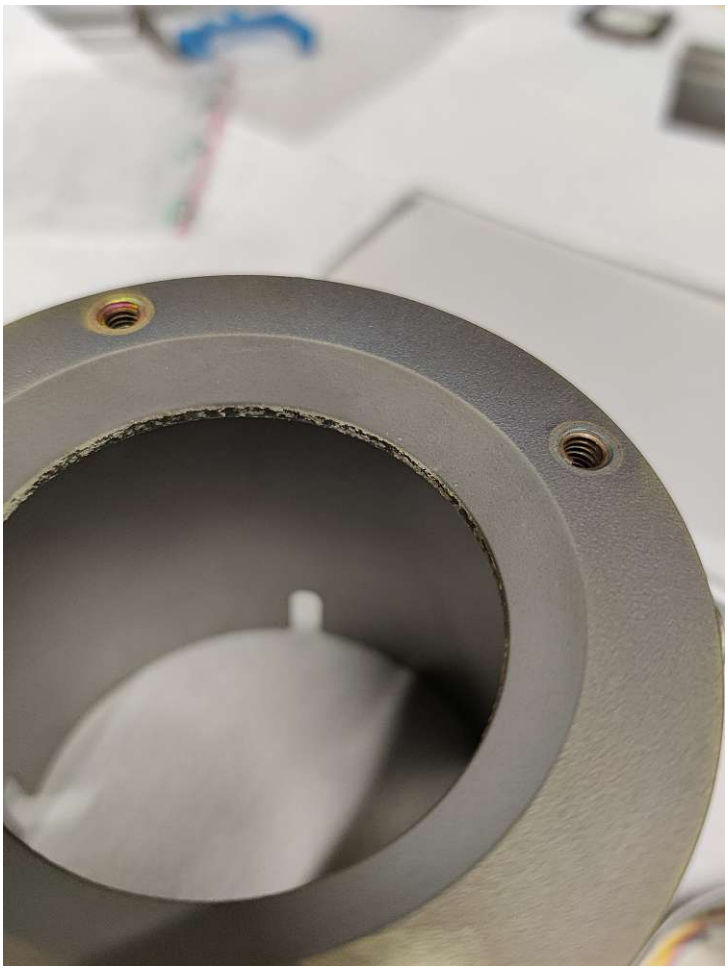

Figure 27: Crumply layer on the containment ring after a 2 h long deposition

A thin layer of titanium nitride was sputtered onto the containment ring in an attempt to reduce the amount of particles dropping onto the target. The result after another 2 h deposition is shown in Figure 28. The coating adheres better, however, crumbs came off very quickly when trying to perform a further deposition without cleaning the ring first. Due to the additional working time, the coating is only feasible when it is necessary to prevent any contamination of the thin film. However, it is possible to generate dense layers despite the particles.

Another problem is the detachment of some thin films during the cleaning process when ethanol is used. This occured during the cleaning of sample YSZ_29 as is shown in Figure 29. This typically starts on the edge of the thin film and the detached area grows during the cleaning process. It also happened with sample YSZ_38. On both of these samples, two YSZ thin films were deposited for 1 h with a thickness of roughly 220 nm per deposition. This issue never arose during the samples deposited with the procedure described in 4.1.4. It is assumed that the reason for this is a diminished adhesion of thinner films to the substrate or Ethanol creeps underneath the deposited layer through a pinhole. Another example is YSZ_12 with only 190 nm where a large area of the thin film detached as well.

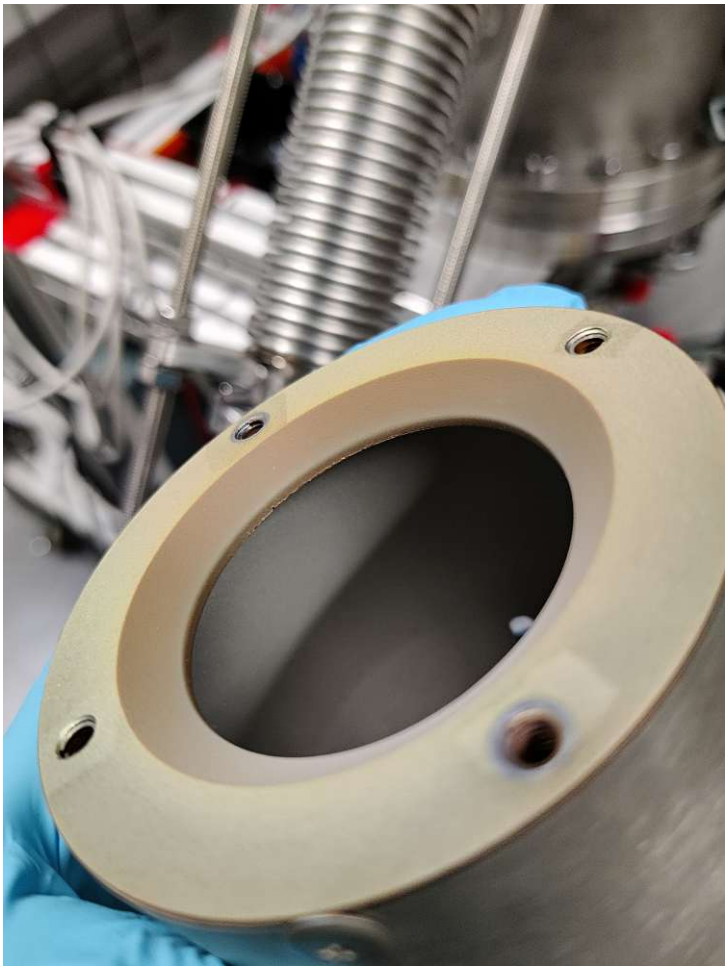

Figure 28: Layer on the titanium nitride coated containment ring.

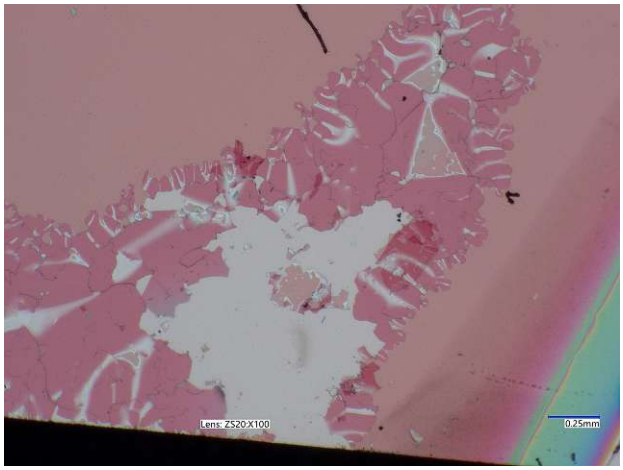

Figure 29: Detached thin film of YSZ_29.

4.2 Characterization

4.2.1 Scanning Electron Microscopy (SEM)

SEM images of the surface and the cross-section of some samples were taken to analyze the structure of the thin films. Figure 30 displays surface images of three samples with different magnifications. The main difference between YSZ_2 and YSZ_22 is a different deposition power 2. Both samples exhibit a grain structure stemming from the columnar film growth. However, it can be seen that the structure of YSZ_22 is denser by comparing 30a with 30b. This is possibly due to the higher energy of the adatoms. The DC sputtered sample YSZ_25 shows a similar surface structure as YSZ_22. In Figure 30b and 30c there are elevations on the surface which are possibly overgrown dust particles or overgrown particles of the ZrO_2 paste.

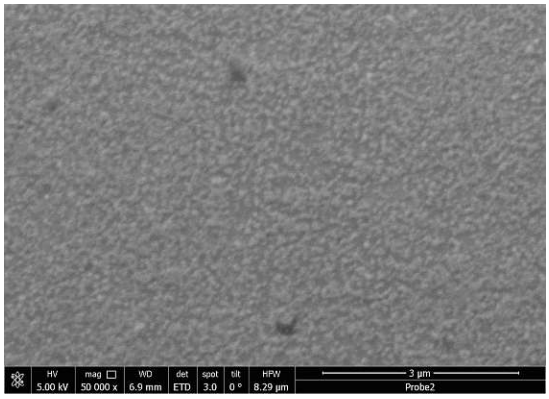

(a) Image of the surface of YSZ_2 (power = 80 W RF, p = 0.33 Pa, O_2/Ar = 1/3).

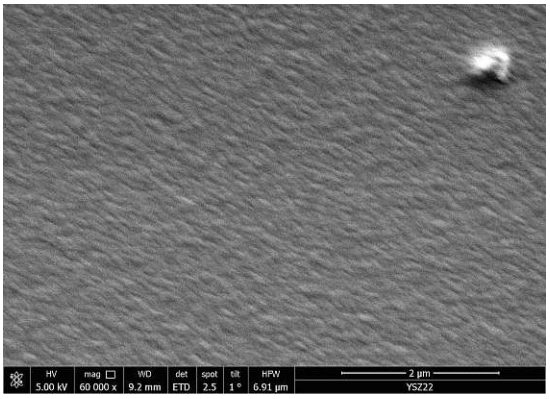

(b) Image of the surface of YSZ_22 (power = 130 W RF, p = 0.451 Pa, O_2/Ar = 1/4).

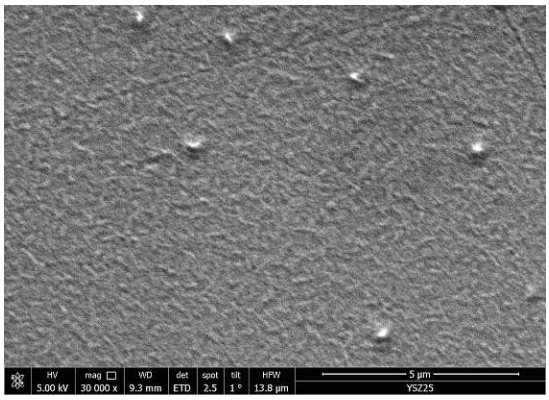

(c) Image of the surface of YSZ_25 (power = 200 W DC, p = 0.5 Pa, O_2/Ar = 1/4).

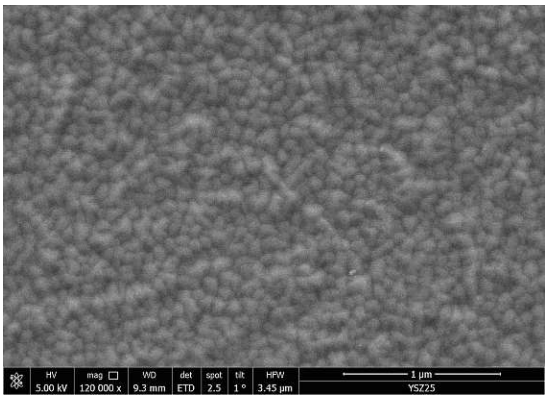

(d) Image of the surface of YSZ_25 (power = 200 W DC, p = 0.5 Pa, O_2/Ar = 1/4).

Figure 30: SEM images of surfaces of different samples.

Figure 31 shows the cross-section of the sample YSZ_23 and YSZ_25. YSZ_25 exhibits a dense columnar growth without visible pinholes due to suboptimal film growth with a thickness of about 830 nm. The image of YSZ_23 is difficult to interpret due to a bad breakage of the sample. However, there are no pinholes visible and the sample is between 373 - 418 nm thick.

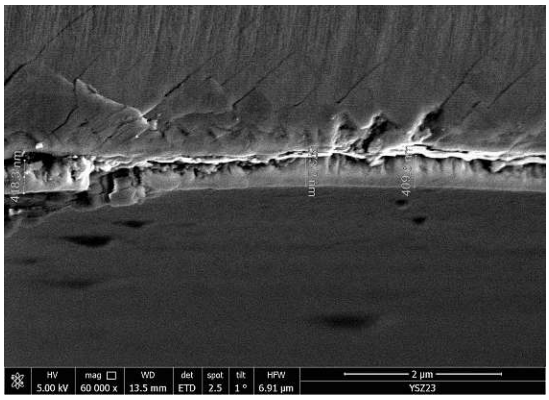

(a) YSZ_23 (power = 130 W, p = 0.295 Pa, O_2/Ar = 1/4).

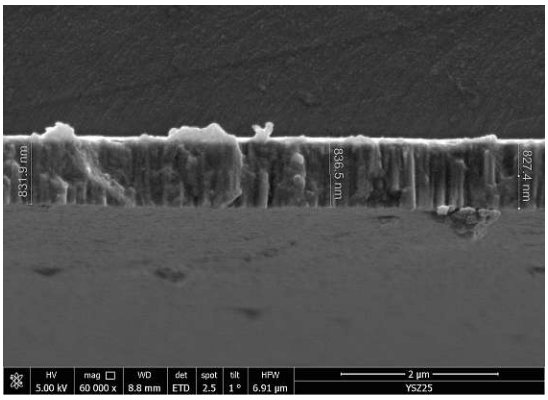

(b) YSZ_25 (power = 200 W DC, p = 0.5 Pa, O_2/Ar = 1/4).

Figure 31: SEM images of cross-sections of different samples.

Figure 32 depicts a cross section of the thin film YSZ_33 which was deposited with the final procedure described in chapter 4.1.4. The YSZ layer is between 804 - 820 nm thick and exhibits a dense columnar growth. Even though the film was deposited in two steps there is no visible boundary between the two YSZ layers.

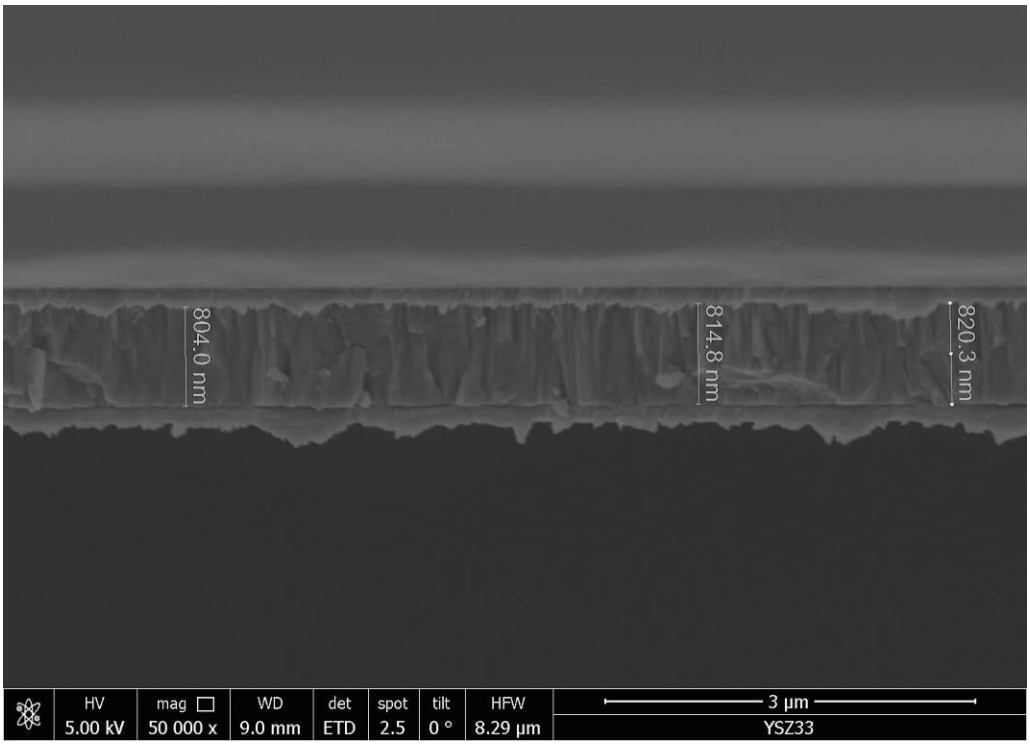

Figure 32: SEM image of the cross-section of YSZ_33 (I = 500 mA DC, p = 0.45 Pa, O_2/Ar = 1/3).

4.2.2 Ionic Conductivity of the YSZ Thin Films

Figure 33 shows EIS spectra of the electrical dense sample YSZ_35, which was deposited in the same manner as YSZ_33, with two Pt electrodes and the resulting fits with the equivalent circle of Figure 34. The semicircle at high frequencies at the left side of the plot is the feature attributed to the YSZ thin film while the low frequency part is due to the Pt electrodes.

The obtained fits closely approximate the characteristic high frequency arc, with the electrode feature exhibiting a more noticeable difference between the fit and the actual data. However, the focus was on a good approximation of the YSZ feature. Based on the data it can be seen that the resistance of the thin film decreases with increasing temperature which is in agreement with the expectation of a thermally activated ion hopping process.

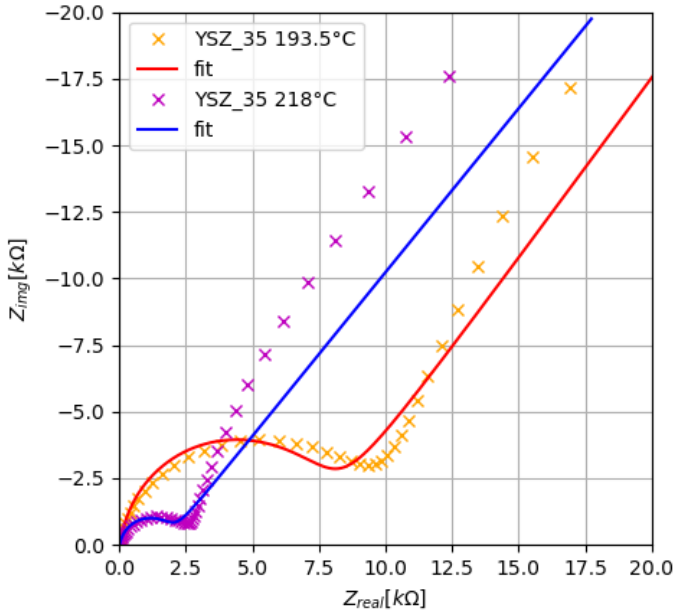

Figure 33: EIS spectra of YSZ_35 at two different temperatures with corresponding fits.

The EIS data were fitted with an equivalent circuit to determine the conductivity of the YSZ thin films. Figure 34 displays the equivalent circuit which was mainly employed. It consists of an inductivity for the cable of the measuring device, a resistance parallel to a constant phase element for the YSZ thin films and in series a resistance parallel to a constant phase element for the Pt electrode.

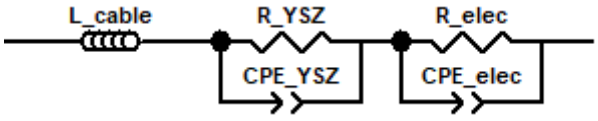

Figure 34: Equivalent circuit for fitting the EIS spectra.

At lower temperatures, it was not possible to fit the data with the equivalent circuit in 34 because the electrode feature was outside of the frequency measuring range. In these

cases, the part describing the electrode in the electrical circuit was omitted. Figure 35 displays an impedance spectra of the sample YSZ_35 with the resulting fit.

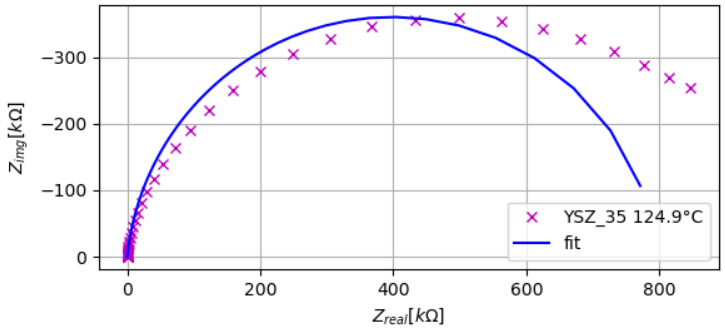

Figure 35: EIS spectra of YSZ_35 with corresponding fit.

At high temperatures, the YSZ feature was not resolved anymore. In these cases, the intersection between the real axis and the impedance spectra was used to estimate the resistance of the YSZ thin films. This value includes the resistance of the measurement setup of about 3 Ω which is still small compared to the resistance of the YSZ thin film in most cases. Figure 36 shows an example spectra at the high-frequency end of YSZ_28 measured with microelectrodes. The spectra were extrapolated to estimate the intercept between the spectra and the real axis.

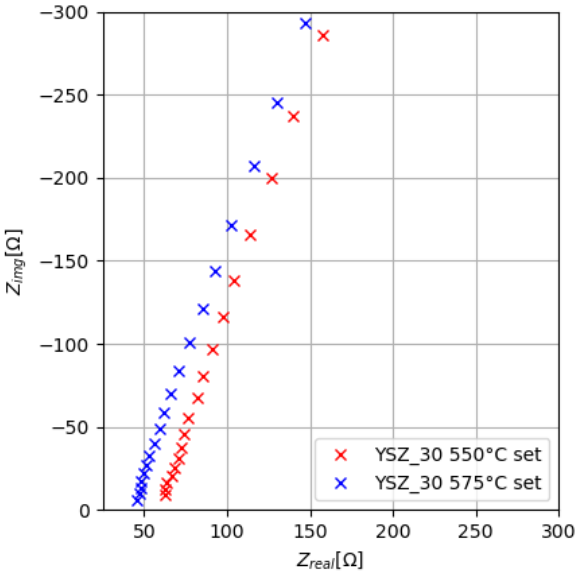

Figure 36: EIS spectra of YSZ_28 at two different heater set temperatures.

The YSZ resistance R_{YSZ} was used to determine the YSZ conductivity σ via $R_{YSZ} = \sigma^{-1}t/A$ (t = thickness, A = area of the electrode). Figure 37 compares the calculated conductivity of various samples against the reference data of a poly-crystalline YSZ sample with 8.04 mol% yttria from [41]. These samples were measured with microelectrodes with asymmetric heating. The conductivity is plotted against the heater set temperature which is higher than the actual sample temperature. Therefore the data should shift to the right when plotted against the actual sample temperature which is unknown. However, all the samples show the expected linear increase in conductivity when $\ln(\sigma T)$ is compared to $1/T$. YSZ_12 has the smallest conductivity which is about one order of magnitude smaller than the other samples. All the remaining samples exhibit a conductivity that closely aligns with the reference data, showing a subtle trend where thicker films tend to have higher conductivity. The good conductivity data indicates that the films have the desired YSZ composition.

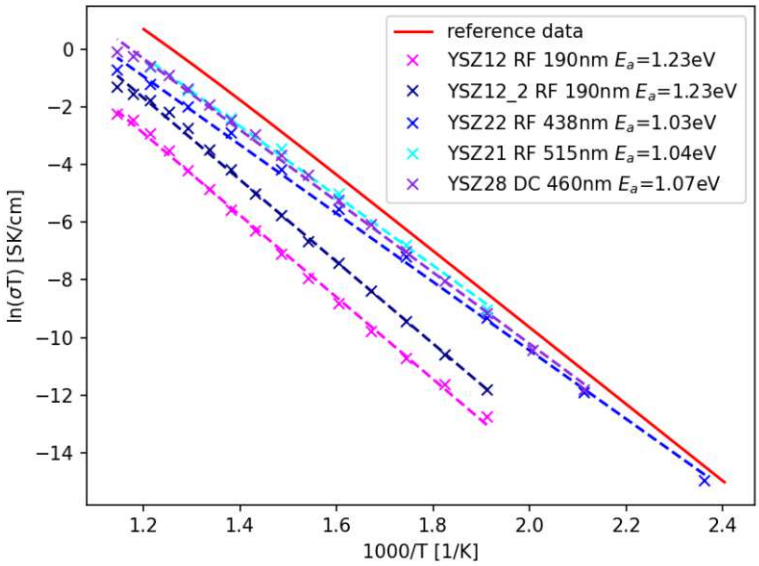

Figure 37: Electric conductivity times T of microelectrodes vs the inverse heater set temperature of various samples with one sputter deposition measured in an asymmetric heater setup compared with reference data of poly-crystalline YSZ sample with 8.04 mol% yttria from [41]. Two different microelectrodes where measured from YSZ_12.

Figure 38 is a plot of $\ln(\sigma T)$ against $1000/T$ of different two times deposited samples compared to reference data of [41]. The samples were measured with a macroelectrode during the heating and during cooling down in the configuration of the symmetric heater and a thermocouple. The conductivities of each sample are similar during heating and cooling down, which indicates that the samples are not altered during the heating process. Only sample YSZ_34 has an outlier which shifts the fitted curve. The samples were sputtered with the same parameters and exhibited a good conductivity compared to the reference data, in particular YSZ_35. This sample even has a slightly higher conductivity at lower temperatures. Please note that, YSZ_34 was sputtered onto LSF with a resistivity of approximately 1 MΩ. This changed the impedance spectra and it was not possible to measure the conductivity of the thin film at high temperatures. An example of the impedance spectra of YSZ_34 and the corresponding fit can be seen in Figure 39. The

equivalent circle of Figure 34 was slightly adapted by changing the impedance with a resistance to take the resistance of the mixed conductor into account.

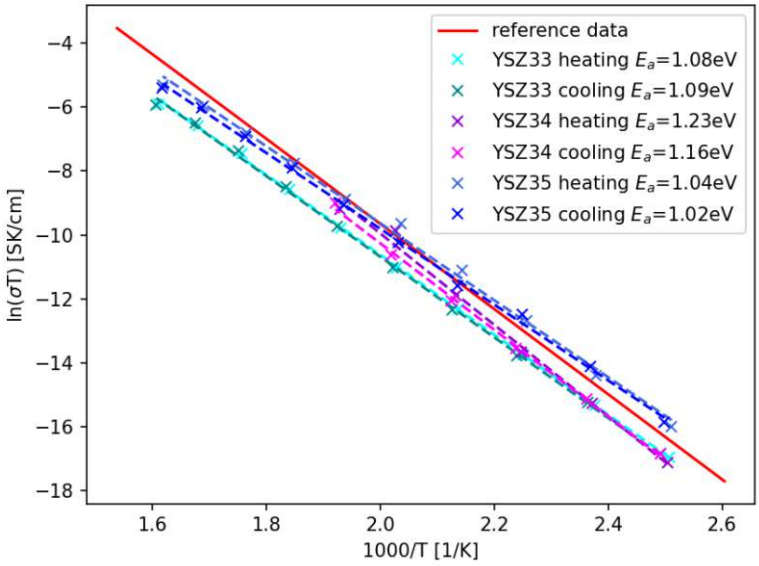

Figure 38: Electric conductivity times T of macroelectrodes vs the inverse temperature of various samples with two consecutive sputter depositions measured in a symmetric heater compared with reference data of poly-crystalline YSZ sample with 8.04 mol% yttria from [41].

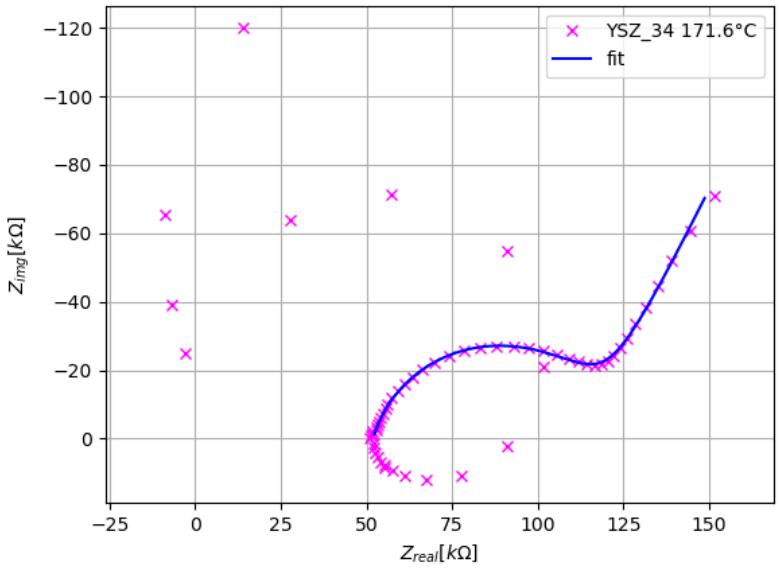

Figure 39: Impedance spectra of YSZ_34 with corresponding fit.

4.2.3 Laser Induced Breakdown Spectroscopy (LIBS)

LIBS measurements were performed to analyze the sample stoichiometry. A YSZ single crystal with 9.5 mol% Y_2O_3 was measured as well as a reference. For the measurement of the single crystal, the laser was aimed at one spot with five separate laser pulses, whereas for the sample the laser was aimed at five different spots with five laser pulses each time. The measured counts per second per laser pulses of Y were divided by the counts of Zr. Then the arithmetic mean was calculated over the five measurements. Table 5 lists the calculated values of each spot and the mean over the spots. Comparing the sample to the reference resulted in 9.3 mol% yttria.

To compare this value to the 15 weight% of Y of the target this value was converted into weight% resulting in 16.7 weight% of Y. This means that during the sputtering process, the yield of Y is higher than the yield of Zr. However, the composition lies within a desired area and is consistent with the good conductivities in chapter 4.2.2.

Table 5: Calculated arithmetic means of each spot for a YSZ single crystal and YSZ_35 rounded to four decimal digits.

	Spot 1	Spot 2	Spot 3	Spot 4	Spot 5	mean
YSZ single crystal	1.1588	-	-	-	-	1.1588
YSZ_35	1.1368	1.0700	1.1706	1.1577	1.1559	1.1382

4.2.4 X-Ray Fluorescence (XRF) spectroscopy

The composition of YSZ_30, sputtered with the parameters in table 4, was measured via XRF and compared to a YSZ single crystal from Crystec with 9.5 mol% of Y_2O_3. The results of the measurements of the sample are shown in table 6. There was also Si observed due to the single crystal substrate and small traces of Zn. Both of these materials were omitted to calculate the percentages of the materials. The Pt signal stems from the electrode and Hf contamination was also observed in the single crystal.

Table 6: XRF measurement of YSZ_30 and the relative percentage of the materials to each other.

O	Y	Zr	Hf	Pt
41.15%	9.689%	46.247%	0.122%	2.792%

The ratio of Y and Zr was calculated for the sample and the reference crystal and then compared. This resulted in 9.4 mol% yttria. This value fits very well with the LIBS measurements of YSZ_35.

4.2.5 Grazing Incidence X-Ray Diffraction

Sample YSZ_35 was analyzed with a grazing incidence X-ray diffraction (GID) with an angle of incidence of 3°. Figure 40 shows the result of the measurement. The sample was compared to a Pt sample from [45] and against a $O_{1.893}Y_{0.214}Zr_{0.786}$ sample from [46]. The four peaks with the highest intensity of Pt were detected due to the Pt electrode. The [111] peak at 39.784°, the [200] peak at 46.244°, the [200] peak at 67.456° and the [311] peak overlapping with a peak of YSZ at 81.289°. The peak with the highest intensity is the [111] peak at 30.046°. This peak also occurs in the measured difractogram but it is slightly shifted to a lower angle. This is possibly due to a different ratio of Y to Zr in the sample compared to the reference data. Furthermore, the [220] peak at 50.083° was also detected with a low intensity. The [311] peak at 59.516° was measured as well and possibly the overlapping [311] peak at 81.433°. This difractogram indicates a polycrystalline film growth of the YSZ thin film.

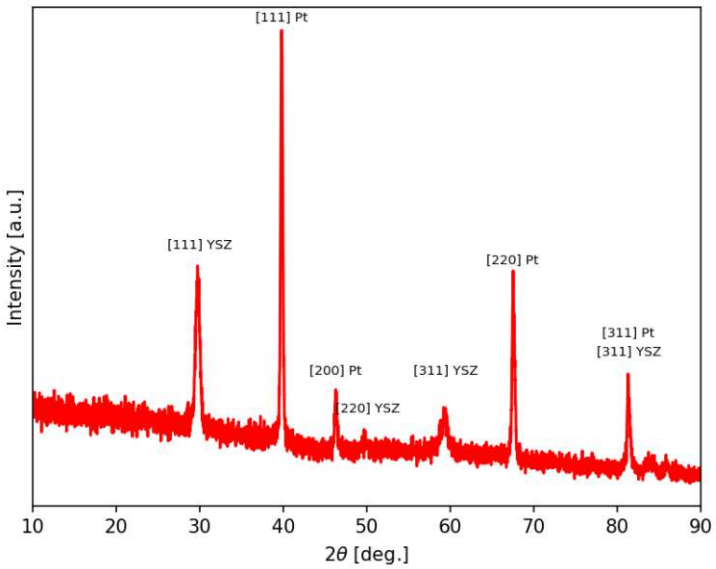

Figure 40: Results of the GID measurement of YSZ_35

4.3 Oxygen Ion Battery (OIB)

Based on the procedure for depositing dense YSZ films, an oxygen ion battery was fabricated with a LSCrMn thin film anode and a LSF thin film cathode. The OIB was measured as described in 3.3.3. Around every 0.5 s the flowing current, the cell voltage between the LSF and LSCrMn electrode and the potential of the LSF electrode against the atmosphere was recorded. The data were sorted into cycles where the battery was first charged and then discharged. The first cycle was discarded due to a different charging behavior directly after equilibrating the sample. In the next step, the charge Q stored/withdrawn was calculated with zero charge at the beginning for discharging and charging. The accumulated charge was calculated by

$$Q_{i+1} = Q_i + |I_i|(t_{i+1} - t_i) \tag{15}$$

with the current I, the time t and the index i. Then the charge was normalized to the size of the electrodes with 49 mm^2. Figure 41 shows the charging and discharging curve of multiple cycles with a current of 10 µA at 350 °C. The battery has a capacity of roughly 9.92 µA h cm^{-2} which results in a capacity of 1.75×10^{-2} C for the whole OIB which decreases slightly with each cycle.

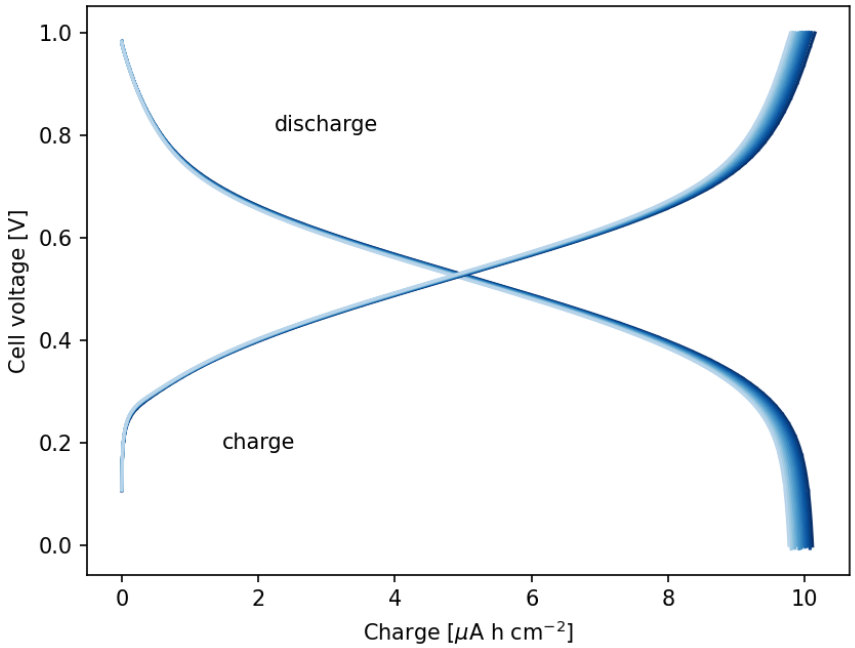

Figure 41: Charging and discharging curve of multiple cycles of the OIB with a current of 10 µA at 350 °C.

Figure 42 displays the change of the capacity of the battery during the cycling. The capacity decreases almost linearly with each cycle. Furthermore, the coloumb efficiency

$$\eta_C = \frac{Q_{discharging}}{Q_{charging}} \tag{16}$$

with $Q_{discharging}$ the amount of charge withdrawn from the battery and $Q_{charging}$ the amount of charge pumped into the battery, is greater than 99.6% for every cycle. It should be emphasized that the presented cell displays the first working thin film oxygen ion battery ever.

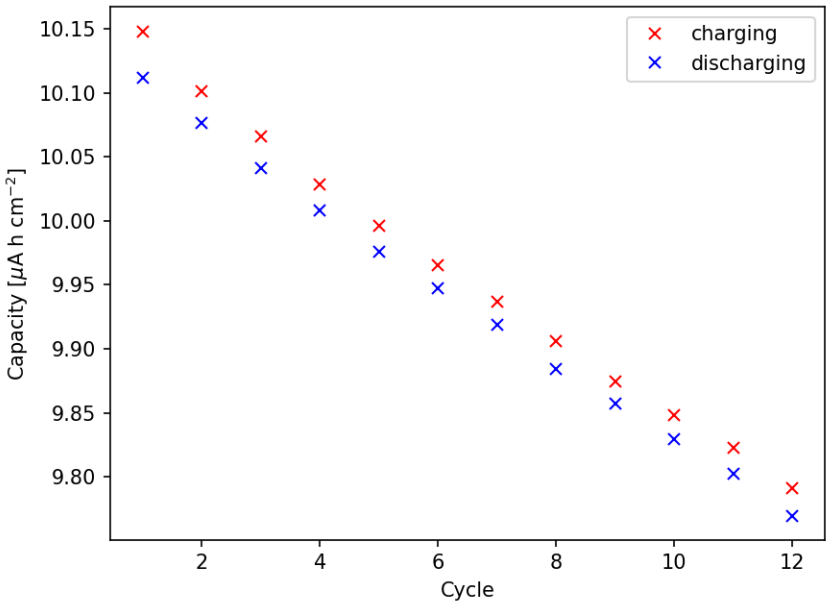

Figure 42: Capacity of the OIB plotted against the cycle number with a current of 10 µA.

Figure 43 shows the LSF potential measured vs. a reference electrode at 0.25 mbar O_2 plotted against the charge over multiple cycles. At a low charge, the course of the potential is almost the same. It only shifts to an increased value with an increasing amount of cycling. Especially during charging, when the battery is almost full, the LSF potential starts to increase rapidly at a lower charge.

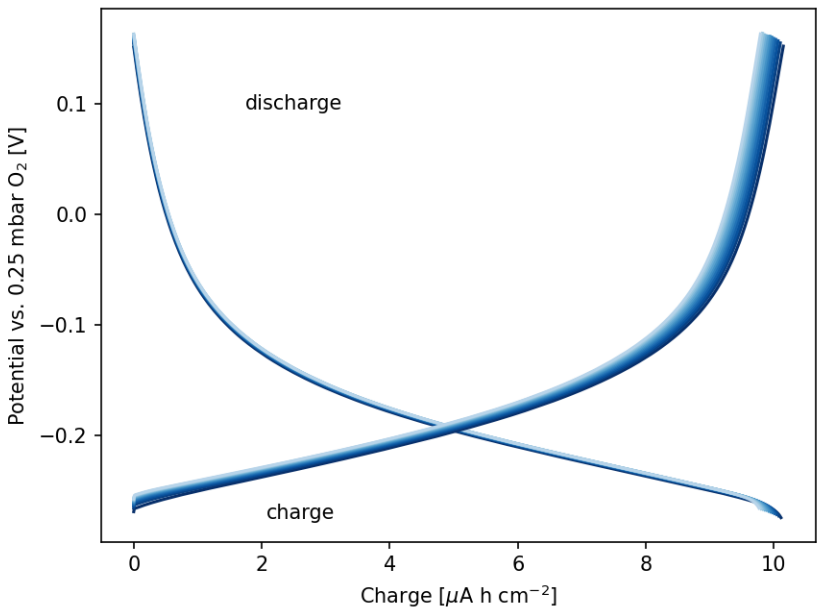

Figure 43: LSF potential vs. 0.05 bar O_2 plotted against the charge over multiple cycles.

The discharge curve can be mirrored by subtracting the withdrawn charge from the charge stored. The overpotential η can then be evaluated by subtracting this new mirrored discharge curve from the charging curve and dividing the result by two. An example result of an overpotential with a current of 10 µA is shown in Figure 44. At first the overpotential is high with 60 mV due to a fully oxidized LSCrMn electrode and a poor ionic conductivity of the electrode. Then the overpotential decreases quickly to only 2.3 mV and is rather stable until the battery is almost completely loaded where the overpotential increases again to over 10 mV likely due to oxidation of the LSF electrode.

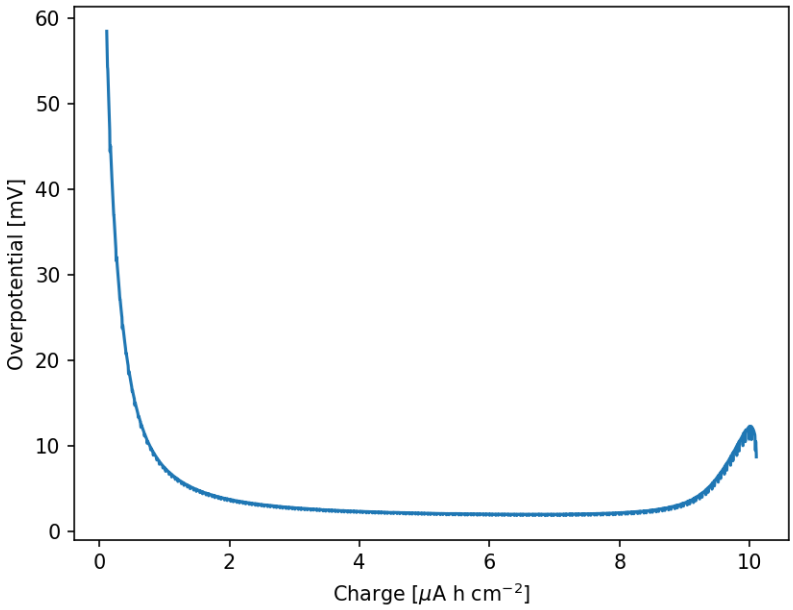

Figure 44: Calculated overpotential of the OIB with a current of 10 µA.

The conductivity of YSZ_35 in chapter 4.2.2 can be used to estimate the portion of the overpotential attributable to the resistance of the YSZ thin film of the OIB, which was deposited with identical parameters. This results in a conductivity of 9.58×10^{-6} S/cm at 350 °C. The film thickness is assumed to be about 814 nm and the active electrode area of 49 mm^2. These values yield a resistance of 17.34 Ω of the YSZ thin film. The expected voltage drop due to the thin film is calculated through multiplication with the charging/discharging current. Figure 45 compares the mean overpotential against the overpotential caused by the YSZ layer of different charging/discharging currents. The mean overpotential is evaluated by forming the arithmetic mean of the overpotential of one charge/discharge curve between the charge of 2.27-7.37 µAh/cm^2 and then calculating the arithmetic mean over all cycles. The overpotential increases linearly with the current which could be described by Ohms law with a resistance of about 88.05 Ω. Less than 19.7% of the overpotential in the region where neither electrode is strongly oxidized stem from the YSZ layer according to this estimation. Hence, another resistance contribution has to come into play and determines the overpotential. Owing to the ohmic character and the small change in the respective voltage range the electrode ionic conductivity is probably not responsible. Rather, the electrode/electrolyte interface might be the reason. However, YSZ and LSF can react at the electrode/electrolyte interface and form the zirconates $La_2Zr_2O_7$ and $SrZrO_3$. These reaction products are insulating and lead to

an increased interface resistance [47]. Therefore, the actual resistance caused by the YSZ layer is higher than expected. An additional ceria layer may mitigate this problem.

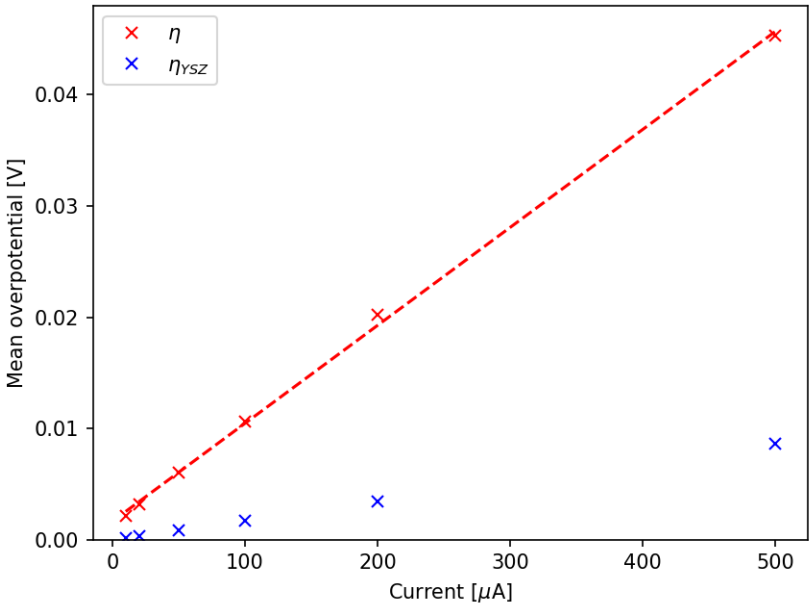

Figure 45: Overpotential of the OIB and the overpotential caused of the YSZ layer plotted against the current.

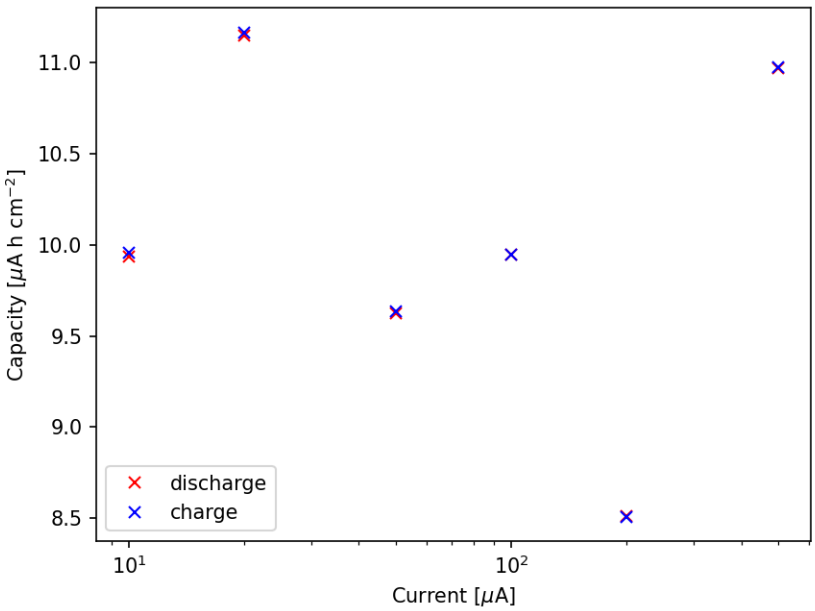

Figure 46: The arithmetic mean of the capacity over the cycles of the OIB plotted against the current.

Figure 46 displays the arithmetic mean of the capacity over the cycles of the OIB plotted against the current. The capacity varies between 0.085×10^{-2}-1.13×10^{-2} mA h cm^{-2} with no visible connection to the current. The difference in capacity is most likely because of

insufficient equilibration with the atmosphere. Figure 47 illustrates that a higher LSF potential at the initiation of the charging process is associated with a lower capacity.

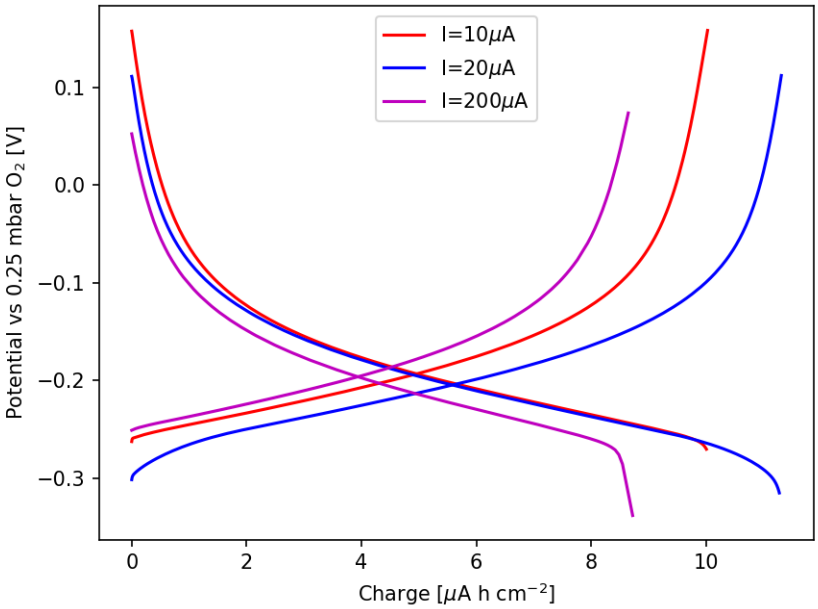

Figure 47: Potential of the LSF electrode against the charge.

All the measurements show that the optimized YSZ thin films of this study can indeed be used in oxygen ion batteries and exhibit very good conduction properties and densities.

5 Summary

In the course of this thesis, two different methods to deposit dense YSZ thin films were tested. One method was RF-sputtering. Through optimization of the sputtering parameters a dense film growth was achieved. The optimized parameters with a metallic target are a plasma power between 130 - 150 W, a pressure between 0.291 - 0.451 Pa, a ratio of Ar to O_2 of 1/5 or 1/4 and a heater set temperature of around 800 °C. Additionally, a dense film growth was obtained with a ceramic target with a plasma power of 140 W, a pressure of 0.4 Pa, a ratio of Ar to O_2 of 1/10 and a heater set temperature of 850 °C. However, only approximately 75 % of the film area was insulating most likely due to dirt particles preventing the film growth on parts of the substrate.

The other deposition method was reactive DC-sputtering. In this case the sputter parameters of current to the target of 500 mA, a pressure of 0.45 Pa, a ratio of Ar to O_2 of 1/3 with the O_2 inlet close to the substrate and a heater set temperature of around 850 °C resulted in a dense film growth. These thin films exhibit an ionic conductivity that closely aligns with the data of bulk samples found in the literature. Furthermore, the stochiometry was investigated via LIBS and XRF measurements. This resulted in an Y_2O_3 content of around 9.3 mol% which is a bit higher than expected from the Y content in the target. However, these layers still contained defects mostly likely due to dirt particles.

In order to reproducibly deposit insulating YSZ thin films over the complete substrate area, a dedicated sputtering procedure was developed. The crucial step involved sputtering two YSZ layers using identical sputtering parameters, stacked on top of each other. In between these two depositions, the sample was cleaned with ethanol and a cleanroom wipe to remove the dirt particles from the sputtered layer. This enabled the second layer to close up the pinholes of the first layer, resulting in an approximately 800 nm insulating thin film.

These dense YSZ thin films were successfully utilized as an electrolyte in a thin film OIB. The battery had a capacity of about 9.92 µA h cm^{-2} with a coloumb efficiency greater than 99.6 %. Less than 20 % of the overpotential of the OIB stem from the YSZ layer at charging/discharging currents up to 500 µA estimated from the ionic conductivity of the thin films. However, the contribution of the thin film to the overpotential could be higher due to unfavorable reactions with the electrode. An additional layer of sputtered gadolinium-doped ceria between the electrodes and the electrolyte could possibly further improve the performance of the OIB.

Danksagung

Zum Abschluss möchte ich mich noch bei einigen Leuten bedanken.

Ein besondere Dank gilt meinen beiden Betreuern Tobias Huber und Alexander Schmid für die Untersützung bei sämtlichen Fragen in Bezug auf die Anlage oder zu den elektrischen Messungen.

Bei Jürgen Fleig bedanke ich mich für die Möglichkeit, meine Diplomarbeit in seiner Forschungsgruppe durchzuführen. Hier danke ich auch der gesamten Arbeitsgruppe für ihre Unterstützung.

Danke an Kirsten Rath für die SEM Aufnahmen, an Maximilian Weiss für die Hilfe bei der XRF Messung und der LIBS Messung und an Andreas Bumberger für die Gracing Incidence Messung

Außerdem danke ich meiner Familie, meinen Freunden und insbesondere meiner Verlobten Medea Karbus für die Unterstützung während meiner gesamten Studienzeit.

References

[1] A. Olabi and M. A. Abdelkareem, "Renewable energy and climate change," *Renewable and Sustainable Energy Reviews*, vol. 158, p. 112 111, 2022.

[2] X. Zhang and I. Dincer, *Energy Solutions to Combat Global Warming*. Springer International Publishing, 2017, vol. 33.

[3] iea. "Report extract Electricity." (2019), [Online]. Available: `https://www.iea.org/reports/world-energy-outlook-2019/electricity`. (accessed: 04.01.2024).

[4] K. Abbass, M. Z. Qasim, H. Song, M. Murshed, H. Mahmood, and I. Younis, "A review of the global climate change impacts, adaptation, and sustainable mitigation measures," *Environmental Science and Pollution Research*, vol. 29, no. 28, pp. 42 539–42 559, 2022.

[5] J. Kotcher, E. Maibach, and W.-T. Choi, "Fossil fuels are harming our brains: identifying key messages about the health effects of air pollution from fossil fuels," *BMC public health*, vol. 19, no. 1079, pp. 1–12, 2019.

[6] A. Hussain, S. M. Arif, and M. Aslam, "Emerging renewable and sustainable energy technologies: State of the art," *Renewable and Sustainable Energy Reviews*, vol. 71, pp. 12–28, 2017.

[7] J. Mermelstein and O. Posdziech, "Development and Demonstration of a Novel Reversible SOFC System for Utility and Micro Grid Energy Storage," *Fuel Cells*, vol. 17, no. 4, pp. 562–570, 2017.

[8] C. Liu, F. Li, L.-P. Ma, and H.-M. Cheng, "Advanced Materials for Energy Storage," *Advanced Materials*, vol. 22, no. 8, E28–E62, 2010.

[9] H. Ishaq, I. Dincer, and C. Crawford, "A review on hydrogen production and utilization: Challenges and opportunities," *International Journal of Hydrogen Energy*, vol. 47, no. 62, pp. 26 238–26 264, 2022.

[10] Y. Haseli, "Maximum conversion efficiency of hydrogen fuel cells," *International Journal of Hydrogen Energy*, vol. 43, no. 18, pp. 9015–9021, 2018.

[11] T. Hai, A. El-Shafay, A. Alizadeh, H. A. Dhahad, B. S. Chauhan, S. F. Almojil, A. I. Almohana, and A. F. Alali, "Comparison analysis of hydrogen addition into both anode and afterburner of fuel cell incorporated with hybrid renewable energy driven SOFC: An application of techno-environmental horizon and multi-objective optimization," *International Journal of Hydrogen Energy*, vol. 51, pp. 1195–1207, 2023.

[12] M. A. Abdelkareem, W. H. Tanveer, E. T. Sayed, M. E. H. Assad, A. Allagui, and S. W. Cha, "On the technical challenges affecting the performance of direct internal reforming biogas solid oxide fuel cells," *Renewable and Sustainable Energy Reviews*, vol. 101, pp. 361–375, 2019.

[13] N. Radenahmad, A. T. Azad, M. Saghir, J. Taweekun, M. S. A. Bakar, M. S. Reza, and A. K. Azad, "A review on biomass derived syngas for SOFC based combined heat and power application," *Renewable and Sustainable Energy Reviews*, vol. 119, p. 109 560, 2020.

[14] R. K. Akikur, R. Saidur, H. W. Ping, and K. R. Ullah, "Performance analysis of a co-generation system using solar energy and SOFC technology," *Energy Conversion and Management*, vol. 79, pp. 415–430, 2014.

[15] E. D. Wachsman and K. T. Lee, "Lowering the temperature of Solid Oxide Fuel Cells," *Science*, vol. 334, no. 6058, pp. 935–939, 2011.

[16] E. Rezugina, A. L. Thomann, H. Hidalgo, P. Brault, V. Dolique, and Y. Tessier, "Ni-YSZ films deposited by reactive magnetron sputtering for SOFC applications," *Surface and Coatings Technology*, vol. 204, no. 15, pp. 2376–2380, 2010.

[17] V. Sinha and S. Mondal, "Recent development on performance modelling and fault diagnosis of fuel cell systems," *International Journal of Dynamics and Control*, vol. 6, pp. 511–528, 2018.

[18] A. Weber, "Fuel flexibility of solid oxide fuel cells," *Fuel Cells*, vol. 21, no. 5, pp. 440–452, 2021.

[19] A. Schmid, M. Krammer, and J. Fleig, "Rechargeable Oxide Ion Batteries Based on Mixed Conducting Oxide Electrodes," *Advanced Energy Materials*, vol. 13, no. 11, p. 2 203 789, 2023.

[20] Y. Yang, Y. Zhang, and M. Yan, "A review on the preparation of thin-film YSZ electrolyte of SOFCs by magnetron sputtering technology," *Separation and Purification Technology*, vol. 298, p. 121 627, 2022.

[21] H. Wang, W. Ji, L. Zhang, Y. Gong, B. Xie, Y. Jiang, and Y. Song, "Preparation of YSZ films by magnetron sputtering for anode-supported SOFC," *Solid State Ionics*, vol. 192, no. 1, pp. 413–418, 2011.

[22] H.-S. Noh, J.-W. Son, H. Lee, H.-S. Song, H.-W. Lee, and J.-H. Lee, "Low Temperature Performance Improvement of SOFC with Thin Film Electrolyte and Electrodes Fabricated by Pulsed Laser Deposition," *Journal of The Electrochemical Society*, vol. 156, no. 12, B1484, 2009.

[23] H. Hidalgo, A.-L. Thomann, T. Lecas, J. Vulliet, K. Wittmann-Teneze, D. Damiani, E. Millon, and P. Brault, "Optimization of DC Reactive Magnetron Sputtering Deposition Process for Efficient YSZ Electrolyte Thin Film SOFC," *Fuel cells*, vol. 13, no. 2, pp. 279–288, 2013.

[24] P. Coddet, M.-L. Amany, J. Vulliet, A. Caillard, and A.-L. Thomann, "YSZ/GDC bilayer and gradient barrier layers deposited by reactive magnetron sputtering for solid oxide cells," *Surface and Coatings Technology*, vol. 357, pp. 103–113, 2019.

[25] R. Nédélec, S. Uhlenbruck, D. Sebold, V. Haanappel, H.-P. Buchkremer, and D. Stöver, "Dense yttria-stabilised zirconia electrolyte layers for SOFC by reactive magnetron sputtering," *Journal of Power Sources*, vol. 205, pp. 157–163, 2012.

[26] M. Ohring, "Discharges, Plasmas, and Ion-Surface Interactions," in *Materials Science of Thin Films - Deposition and Structure*, 2nd Edition, Elsevier, 2002, pp. 145–202.

[27] D. M. Mattox, "Chapter 7 - Physical Sputtering and Sputter Deposition (Sputtering)," in *Handbook of Physical Vapor Deposition (PVD) Processing*, Second Edition, Elsevier Inc, 2010, pp. 237–286.

[28] P. J. Kelly and R. D. Arnell, "Magnetron sputtering: a review of recent developments and applications," *Vacuum*, vol. 56, no. 3, pp. 159–172, 2000.

[29] M. S. Raven, "Radio frequency sputtering and the deposition of high-temperature superconductors," *Journal of Materials Science: Materials in Electronics*, vol. 5, pp. 129–146, 1994.

[30] A. Anders, "Physics of arcing, and implications to sputter deposition," *Thin Solid Films*, vol. 502, no. 1-2, pp. 22–28, 2006.

[31] Y. Lim, S. Hong, J. Bae, H. Yang, and Y.-B. Kim, "Influence of deposition temperature on the microstructure of thin-film electrolyte for SOFCs with a nanoporous AAO support structure," *International Journal of Hydrogen Energy*, vol. 42, no. 15, pp. 10 199–10 207, 2017.

[32] E. M. Mills, M. Kleine-Boymann, J. Janek, H. Yang, N. D. Browning, Y. Takamura, and S. Kim, "YSZ thin films with minimized grain boundary resistivity," *Physical Chemistry Chemical Physics*, vol. 18, no. 15, pp. 10 486–10 491, 2016.

[33] P. Briois, E. Gourba, A. Billard, A. Ringuedé, and M. Cassir, "Microstructure — Electrical properties relationship of YSZ thin films reactively sputter-deposited at different pressures," *Ionics*, vol. 11, pp. 301–305, 2005.

[34] S. Hong, D. Lee, Y. Lim, J. Bae, and Y.-B. Kim, "Yttria-stabilized zirconia thin films with restrained columnar grains for oxygen ion conducting electrolytes," *Ceramics International*, vol. 42, no. 15, pp. 16 703–16 709, 2016.

[35] A. H. Simon, "Chapter 7 - Sputter Processing," in *Handbook of Thin Film Deposition*, Fourth Edition, Elsevier Inc, 2018, pp. 195–230.

[36] F. Smeacetto, M. Salvo, L. C. Ajitdoss, S. Perero, T. Moskalewicz, S. Boldrini, L. Doubova, and M. Ferraris, "Yttria-stabilized zirconia thin film electrolyte produced by RF sputtering for solid oxide fuel cell applications," *Materials Letters*, vol. 64, no. 22, pp. 2450–2453, 2010.

[37] C.-h. Park, Y. H. Kim, H. Jeong, B.-R. Won, H. Jeon, and J.-h. Myung, "Development of robust YSZ thin-film electrolyte by RF sputtering and anode support design for stable IT-SOFC," *Ceramics International*, vol. 49, no. 20, pp. 32 953–32 961, 2023.

[38] A. Shaula, J. Oliveira, V. Kolotygin, C. Louro, V. Kharton, and A. Cavaleiro, "Protective YSZ-based thin films deposited by RF magnetron sputtering," *Vacuum*, vol. 83, no. 10, pp. 1266–1269, 2009.

[39] S. Rey-Mermet, Y. Yan, C. Sandu, G. Deng, and P. Muralt, "Nanoporous YSZ film in electrolyte membrane of Micro-Solid Oxide Fuel Cell," *Thin Solid Films*, vol. 518, no. 16, pp. 4743–4746, 2010.

[40] L. Malavasi, C. A. Fisher, and M. S. Islam, "Oxide-ion and proton conducting electrolyte materials for clean energy applications: structural and mechanistic features," *Chemical Society Reviews*, vol. 39, no. 11, pp. 4370–4387, 2010.

[41] C. Ahamer, A. K. Opitz, G. Rupp, and J. Fleig, "Revisiting the Temperature Dependent Ionic Conductivity of Yttria Stabilized Zirconia (YSZ)," *Journal of The Electrochemical Society*, vol. 164, no. 7, F790, 2017.

[42] D. M. Smyth, *The Defect Chemistry of Metal Oxides*. Oxford University Press, 2000.

[43] F. Ciucci, "Modeling electrochemical impedance spectroscopy," *Current Opinion in Electrochemistry*, vol. 13, pp. 132–139, 2019.

[44] G. Instruments. "Basics of Electrochemical Impedance spectroscopy." (2010), [Online]. Available: `https://www.gamry.com/assets/Application-Notes/basics-of-electrochemical-impedance-spectroscopy.pdf`. (accessed: 24.11.2023).

[45] H. Swanson and E. Tatge, "Natl. Bur. Stand.(US), Circ. 539," 1953.

[46] I. O. Fábregas, D. G. Lamas, L. Acuña, N. W. de Reca, A. F. Craievich, M. C. d. A. Fantini, and R. Prado, "Crystal structure and local order of nanocrystalline zirconia-based solid solutions," *Powder Diffraction*, vol. 23, no. S1, S46–S55, 2008.

[47] S. He, M. Saunders, K. Chen, H. Gao, A. Suvorova, W. D. Rickard, Z. Quadir, C. Cui, *et al.*, "A FIB-STEM study of Strontium Segregation and Interface Formation of Directly Assembled $La_{0.6}Sr_{0.4}Co_{0.2}Fe_{0.8}O_{3-\delta}$ Cathode on Y_2O_3-ZrO_2 Electrolyte of Solid Oxide Fuel Cells," *Journal of The Electrochemical Society*, vol. 165, no. 7, F417, 2018.